**UNIVERSITY OF THESSALY**

**POLYTECHNIC SCHOOL**

**DEPARTMENT OF MECHANICAL ENGINEERING**

**LABORATORY OF MATERIALS**

**Diploma Thesis**

## Effect of Aging on Corrosion-induced Hydrogen Trapping of Aluminum Alloy 2024

By

Charilaos Karantonidis

Supervisor:

Dr. Helen Kamoutsi

Submitted for the Partial Fulfillment

of the requirements for the degree of

Diploma in Mechanical Engineering

Volos

2017

UNIVERSITY OF
THESSALY

**Certified by the members of the Thesis Committee:**


First examiner

(Supervisor)

Dr. Helen Kamoutsi

Lab Teaching Staff, Department of Mechanical Engineering,

University of Thessaly


Second Examiner

Dr. Gregory Haidemenopoulos

Professor, Department of Mechanical Engineering,

University of Thessaly


Third Examiner

Dr. Vasilis Bontozoglou

Professor, Department of Mechanical Engineering,

University of Thessaly

# Acknowledgments

This project is accomplished in the scope of partial fulfilment of the requirements for the degree of Diploma in Mechanical Engineering at University of Thessaly.

For the completion of this Thesis, I would like to thank my thesis supervisor, Dr. Helen Kamoutsi whose expertise, valuable suggestions, comments, guidance and patience further considerably  my knowledge, as well as for the support over this semester.

Furthermore, very special thanks go to Professor Gregory Haidemenopoulos and Professor Vasilis Bontozoglou for accepting to be the referees of this work.

I would also like to thank Dr. Helen Kamoutsi as well as Professor Gregory Haidemenopoulos for giving me the opportunity in the current Thesis to deal with such an interesting topic.

I would also like to express my very great appreciation to Professor Vasilis Bontozoglou for the concession of his laboratory in the scope of the conduction of experimental procedures for this Thesis.

I wish to acknowledge the help provided by graduate student Panagiotis Floratos for the valuable guidance in the beginning of this project.

Last but not least, special recognition goes to my family and all my friends for their continuous support and encouragement during this study.

Charilaos Karantonidis

# Abstract

Corrosion presents a major concern to the structural integrity of aging aircraft structures and in many other applications. The effect of corrosion on the damage tolerance ability of advanced aluminum alloys calls for a very diligent consideration of the problems associated with the combined effect of corrosion and embrittling mechanisms. The present thesis is a continuation on previous work performed in the Laboratory of Materials that connected corrosion attack with hydrogen embrittlement in aluminum alloy 2024. The present work focuses the effect of aging temperature and duration on corrosion-induced hydrogen trapping of Al alloy 2024 and tries to answer key questions on how the microstructural characteristics of the alloy interact with the produced hydrogen.

The experimental procedures involved the following actions: (1) thermal treatment comprising solid solution, quenching and artificial aging of the specimens (SQA), (2) accelerated corrosion testing (using the EXCO procedure), (3) detailed microstructural investigation of the evolution of corrosion damage by employing metallographic techniques, (4) hydrogen measurements by employing an in-house thermal desorption – gas chromatography system.

The major results reached are the following:

Precipitate free zones were observed along the grain boundaries of specimens of alloy 2024 when aged at 210°C for varying times with respect to the as received material. These areas affect corrosion behavior of the material studied as well as hydrogen uptake.

Corrosion damage in the alloy starts with pitting and develops to a network of intergranular corrosion leading to exfoliation of material. An increase in aging time leads to an initial increase in the depth of attack and weight loss which is followed by a plateau.

Hydrogen is produced during the corrosion process and is being trapped in distinct energy states, which correspond to different microstructural traps. These traps are activated and liberate hydrogen at different temperatures. In alloy 2024, four traps T1 to T4 were identified. Trap T1 is considered to be a reversible trap, which liberates hydrogen continuously at low temperatures. Traps T2, T3 and T4 saturate with exposure time and are considered to be irreversible. As discussed in previous work trapping state T1 corresponds to hydrogen at interstitial sites. Trapping state T4 is the strongest trap and its temperature range corresponds to the dissolution of the strengthening precipitate in alloy 2024.

The study of artificial aging for alloy 2024 revealed that after solid solution and aging at 170°C the maximum peak for the mechanical properties (microhardness, yield) of the alloy is reached after aging between 9 and 15 hours. In the case of aging at 210°C the maximum peak for the mechanical properties (microhardness) of the alloy is reached after aging between 4 and 6 hours.

The behavior of the T2 trapping state is connected to the peak hardness of the materials. Hydrogen is attracted to the strain fields associated with coherent and semi-coherent interfaces. As the particle size increases with aging time, the hardness increases due to coherency hardening, at the same time $H_2$

increases. After the peak, the interfaces loose coherency and the strain fields diminish. The hardness drops and follows Orowan-mechanism. At the same time, $H_2$ drops since $H_2$ is absorbed to the T4 state.

Trapping state T4 which is the strongest trap and its temperature range corresponds to the dissolution of the strengthening precipitate in alloy 2024, is associated with S particles. During aging at $210^{o}C$ the super saturation of solid solution is smaller than when aging at $170^{o}C$, thus the anticipated volume fraction of the S phase is also smaller.

This result is a major breakthrough as it helps elucidate the effect of different precipitates on hydrogen trapping in aluminum alloy 2024, especially at state T2 and T4.

## Table of Contents

## List of Figures

## List of Tables

# Chapter 1- Introduction

## Description of the problem

The importance of corrosion implies a major concern to the structural integrity of aging aircraft structures. As the time of an aircraft in service increases, there is an important probability that corrosion will interact with other forms of damage, such as single fatigue cracks or multiple-site damage in the form of widespread cracking at regions of high stress gradients, it can result in loss of structural integrity and consequently leading to fatal consequences. Thus, the effect of corrosion on the damage tolerance ability of advanced aluminum alloys acquires for a very diligent consideration of the problems associated with the combined effect of corrosion damage and embrittling mechanisms. There has been so far, an increasing attention of research and development concerning structural integrity taking into consideration the related corrosion aspects. It has been realized that the establishment of damage functions for quantifying the accumulation of corrosion and fatigue induced damage is very complex. Therefore, despite the study advancements in modelling fatigue crack growth and multiple-site damage phenomena, the assessment of structural degradation is still relying mainly on test data. [1-3].

To face the corrosion induced structural degradation, available data usually refer to accelerated laboratory corrosion test and rarely to in nature atmospheric or marine exposure corrosion tests. These tests are used for evaluating the corrosion susceptibility of the material by measuring weight loss, as well as, depth and type of corrosion attack. The referred methodology, toward understanding corrosion susceptibility of a material, does not relate corrosion to its effect on the mechanical behavior and residual properties of material. So, it is exactly these missing data that are valuable for facing structural integrity problems of corroded aircraft components. Corrosion- induced mechanical degradation studies have been based mainly on the results of stress corrosion cracking tests [4, 5] or, more rarely on the results of fatigue tests performed in the presence of a corrosive environment [1-3]. Both types of tests provide useful results; they refer, however, to the case where a material is loaded in a corrosive environment but not to situations where a corroded material is subjected to mechanical loads. Present-day considerations of the corrosion-induced structural degradation relate the presence of corrosion with a decrease of the load-bearing capacity of the corroded structural member [2, 6]. This decrease is associated with the presence of corrosion notches that lead to local increase of stress promoting fatigue crack initiation as well. In addition, corrosion-induced reduction of the members' load-bearing thickness which, in the case of the thin alloy skin sheets, may be essential, can lead to appreciable increase of stress gradients [6]. Corrosion-induced material embrittlement is not accounted for. The above consideration of the corrosion-induced structural integrity issue is consistent with the classical understanding of the corrosion attack of aluminum alloys as the result of complex oxidation processes at the materials surface.

The above considerations gain particular importance if the so-called ''aging aircraft'' issue is supposed. The aging aircraft has accumulated corrosion damage during the service life and its residual life depends on degradation by corrosion-induced embrittling mechanisms.

The ''aging aircraft'' issue was determined for a variety of previous studies by the long series of experiments, conducted at the University of Patras [7, 8], on mechanical testing of precorroded (in EXCO) alloy 2024. It was shown that degradation of ductility increases with corrosion exposure time and removal of the corrosion layer restores strength but not ductility. These results indicated the operation of a corrosion-induced embrittlement mechanism. From previous work performed in the Laboratory of Materials [9-11], showed that hydrogen is produced during the corrosion process and is being trapped in distinct energy states, which correspond to different microstructural traps. These traps are activated and liberate hydrogen at different temperatures. In alloy 2024, four traps T1 to T4 were identified. Trap T1 is considered to be a reversible trap, which liberates hydrogen continuously at low temperatures. Traps T2, T3 and T4 saturate with exposure time and are considered to be irreversible. The hydrogen front advances with the corrosion front, so hydrogen penetrates deep in the material through the intergranular paths generated by the corrosion process. Then hydrogen diffuses further in the material establishing a hydrogen-affected zone beneath the corrosion depth of attack. Trapping state T1 was attributed to hydrogen at interstitial sites. Trapping state T4 as the strongest trap was attributed to the strengthening precipitate S in alloy 2024 and state T3 was connected with dislocations present in the material.

## Thesis objectives

In view of the above considerations, the present thesis tries to further elucidate the effect of the microstructural characteristics of the material on hydrogen trapping.

Therefore the main objectives of this thesis are the following:

1) To establish a correlation, if any, between corrosion and precipitate population.
2) To establish a correlation, if any, between precipitate population and hydrogen trapping/uptake.

## Thesis methodology

Research was focused on aircraft aluminum alloy 2024 in the T351 temper. The experimental procedures involved the following actions:

1) Heat treatments,
2) Accelerated corrosion testing with EXCO procedure,

3) Detailed microstructural investigation of the evolution of corrosion damage by employing metallography,
4) Hydrogen measurements by employing an in-house thermal desorption gas chromatography system.

## Thesis outline

The thesis outline is as follows:

Chapter2 - Literature review

Chapter3 - Experimental procedures

Chapter 4 - Results and Discussion

Chapter 5 - Conclusions

Chapter 6 - Proposed Future Work

# Chapter 2 - Literature Review

In the following pages the bibliographic review is presented, aiming at presenting the state of the art for the subject, as well as, discussing the key subjects of this thesis. The review starts with a brief introduction on aluminum alloys (age hardening, damage tolerance). It continues with a discussion of corrosion of aluminum alloys, emphasizing the forms of corrosion (pitting, intergranular corrosion, stress corrosion cracking and exfoliation). Finally there is a discussion of hydrogen damage in alloys and more specifically hydrogen embrittlement of aluminum alloys.

## 2.1 The aircraft aluminum alloys of the 2xxx series

### Microstructure and hardening processes

Alloy 2024 belongs to the 2xxx series of Al-Cu-Mg heat treatable aluminum alloys and has replaced alloy 2017 (Duralumin) as the predominant aircraft alloy. Its widespread applications stem from the excellent combinations of specific strength and fatigue resistance.

Aluminum alloy 2024 in the form of sheet or plate is extensively used in the aircraft industry for fuselage structures, wing tension members, wing and fuselage skins as well as in shear webs and ribs where stiffness, strength and high fatigue performance are required. The chemical composition limits are shown in Table 2. 1 while the tensile mechanical properties are depicted as a function of temper condition and thickness in Table 2. 2.

Table 2. 1: Chemical composition (wt. %) of 2024 aluminum alloy. Source: Alloy 2024

| Element | Cu | Fe | Si | Zn | Ti | Mn | Mg | Cr | Others Total |
|---------|------|------|------|------|------|--------|---------|------|--------------|
| wt. % | 3.8-4.9 | 0.50 | 0.50 | 0.25 | 0.15 | 1.2-1.8 | 1.2-1.8 | 0.10 | 0.15 |

Table 2. 2: Mechanical properties of aluminum alloy 2024, Source: Alloy 2024 ALCOA data sheet.

| Temper | Thickness (mm) | Tensile Strength (MPa) | Yield Strength (MPa) | Elongation (%) |
|---|---|---|---|---|
| 0-Sheet & plate | 0.25-12.44 | 220 | 96 | 12 |
| T3-Flat Sheet | 0.203-6.32 | 434-441 | 289 | 10-15 |
| T351-Plate* | 6.35-101.60 | 441-393 | 289-282 | 12-4 |
| T4-Coiled Sheet | 0.254-3.16 | 427 | 276 | 12-15 |
| T81-Flat Sheet | 0.254-6.32 | 462 | 400 | 5 |
| T851-Plate | 6.35-38.07 | 462-455 | 400-393 | 5 |
| *Strength Decreases as thickness increases | | | | |

The remarkable properties of the 2024 alloy are achieved through age hardening. The heat treatment normally involves three stages: (a) Solution treatment at a temperature within the single-phase α region in order to dissolve all the alloying elements, (b) quenching to room (or lower) temperature, to obtain a supersaturated solid solution (SSSS) and (c) natural or artificial aging for the decomposition of the supersaturated solid solution, in order to form finely dispersed precipitates for precipitation hardening. The precipitation sequences of both binary Al-Cu and ternary Al-Cu-Mg alloys are the following [12-24].

$$SSSS \rightarrow GP \rightarrow \theta'' \rightarrow \theta' \rightarrow \theta \ (CuAl_2) \text{ for Al-Cu alloys}$$
$$SSSS \rightarrow GPB \rightarrow S' \rightarrow S \ (CuMgAl_2) \text{ for Al-Cu-Mg alloys}$$
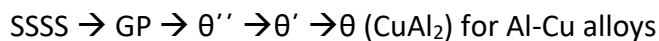
Both of the above precipitation sequences involve the formation of fully coherent GP copper zones (Guinier-Preston zones) or GBP copper-magnesium zones (Guinier-Preston-Bagariatsky zones). These zones evolve during aging to semicoherent intermediate phases ($\theta''$, $\theta'$ or $S'$) and to the final equilibrium incoherent precipitates $\theta$ ($CuAl_2$) or S ($CuMgAl_2$) for the binary Al-Cu and ternary Al-Cu-Mg alloys respectively. In some cases the alloys are cold worked (e.g. by stretching 5%) after quenching and before aging, thus increasing dislocation density and providing more sites for heterogeneous nucleation of intermediate precipitates.

## Corrosion and Residual life

The advantage of the damage tolerant design philosophy is obviously the ability to treat cracked objects in a direct and appropriate fashion. The previous methods only allow for the immediate removal of cracked structure. Use of the stress-intensity values and appropriate data (properties) allows the number of cycles of crack growth over a range of crack sizes to be estimated and fracture

to be predicted. The clear tie of crack size, orientation, and geometry to non-destructive evaluation (NDE) is also a plus. Disadvantages are: possibly computationally intensive stress-intensity factor determinations, greater complexity in development and modelling of property data, and the necessity to perform numerical integration to determine crack growth. In addition, the predicted lives are considerably influenced by the initial crack size used in the calculation, requiring quantitative development of probability of detection for each type of NDE technique employed. Related to the initial crack size consideration is the inability of this approach to model effectively that the component was actually suitable for modelling as a continuum, which eliminates the so-called "initiation" portion of the part life. It becomes obvious that complete knowledge of preexisting cracks and their propagating paths must be available.

A major factor introducing cracks in materials is corrosion that produces cracking of metals as a result of exposure to the aggressive environment. This cracking may take the form of relatively slow, stable crack extension or, as is often the case, unpredictable catastrophic fracture. Investigations involving information on the residual mechanical properties of a structural material following exposure to corrosive environment were conducted by Pantelakis et al. [7, 8], and the effect of corrosion and hydrogen embrittlement on the mechanical behavior of aluminum aircraft alloys was investigated. The work was based on extended, experimental data of the aircraft aluminum alloy 2024. Evaluation of corrosion resistance was performed based on the metallography. As well, the obtained results were discussed under the viewpoint of hydrogen embrittlement.

## 2.2 The corrosion of high-strength aluminum alloys

Regarding corrosion resistance, it is well known that aluminum forms a strongly bonded protective oxide film when exposed to the atmosphere, which when damaged reforms immediately in most environments. This film passivates aluminum in the pH range of about 4 to 8.5. Beyond these limits, aluminum corrodes in aqueous solutions because its oxides are soluble in many acids and bases, yielding $Al^{3+}$ ions in the former and $A1O_2^-$ (aluminate) ions in the latter [25].

### Corrosion of 2024 aluminum alloy

Aluminum alloy 2024 is susceptible to atmospheric corrosion in industrial or coastal areas. Therefore these alloys should be protected when exposed to these conditions. Alloy 2024 can be protected by a thin coating of pure aluminum or corrosion-resistant aluminum alloy, the resulting product is called al-clad 2024 alloy. This cladding is metallurgically bonded to one or both sides of the sheet or plate and may be 1.5-10% of its overall thickness. Any corrosion that might occur, propagates only to the cladding-core interface and then spreads laterally, thus making cladding very effective in providing cathodic protection to the core alloy.

## Pitting corrosion

Alloy 2024 is less corrosion-resistant than other aluminum alloys with lower amounts of copper. Copper's inhomogeneous distribution in the matrix results in pitting and stress corrosion cracking [26-28]. From studies in different corrosive environments it was concluded that $Cl^-$ ion is the most aggressive ion leading to pitting corrosion [29]. Due to the intense presence of $Cl^-$ ions, the marine environment is highly corrosive [30]. The mechanism involves adsorption of $Cl^-$, formation of intermediate complexes and soluble species, thinning of the oxide film, and finally direct attack on the core metal [31]. Contributing to the initiation of corrosion are also the second phase particle present in 2024, mainly the S phase ($CuMgAl_2$) and the $(Cu, Mn, Fe)Al_6$ and/or $Cu_2FeAl_2$ particles [32, 33]. Pits usually first appear on grain boundaries, by selective dissolution of particles, if the boundary precipitates are anodic with respect to the matrix and the precipitate free zone. In the opposite case, the neighboring area poor in compound elements is attacked [34]. Pitting on grain boundaries due to selective generation of anodic regions has been reported in [35-37]. The anodic nature of grain boundaries has also been attributed to the segregation in these regions, with regard to the grain interior where galvanic cells are activated [38].

## Intergranular corrosion

Intergranular corrosion is another form of corrosion of 2024 alloy, which has been the subject of numerous investigations, especially for the classical composition of Al-4%Cu alloys [39]. Intergranular corrosion has been attributed to the difference in the breakdown potentials of $Al_2Cu$ particles along the grain boundaries of aged alloy Al-4%Cu, and the surrounding Cu-depleted zones, which contain only 0.2%Cu [40]. After the dissolution of the grain boundary precipitates, the boundaries are susceptible to corrosion because they are more anodic in comparison to the rest of the matrix [41]. Investigations of Al-4 wt.% Cu foils demonstrated that the alloy was more susceptible to intergranular corrosion in the underaged condition [37]. The intergranular corrosion is possibly linked to pitting corrosion, subsequently pitting formation and pit coalescence at the grain boundary lead to intergranular corrosion.

## Exfoliation corrosion

Alloy 2024 is also susceptible to exfoliation corrosion, which is highly influenced by the environmental conditions. It has been shown that forged truck wheels made of 2024-T4 exfoliate severely in only one or two years in areas, where de-icing salts are used on the highways during the winter months [42]. Mainly responsible for the development of this type of corrosion are the compositional variations present, due to grain boundary precipitation discussed previously. The elongated grains and the directionality of the microstructure have a detrimental effect on the development of intergranular cracks typical of exfoliation corrosion [43-46]. It has been shown that in a 2B06 alloy (similar to 2024), exfoliation corrosion initiated from hydrogen-assisted intergranular cracks when the material was exposed to tropical marine atmosphere [47].

## Stress corrosion cracking and Corrosion fatigue

In the presence of high stresses, 2024 alloy is subjected to stress corrosion cracking (SCC) [48]. Environments that cause SCC are usually aqueous and the presence of a specific chemical species usually chloride ions is essential [49, 50]. Over the years, a large number of possible mechanisms for SCC have been proposed. The most commonly accepted mechanism for SCC in Al-Cu-Mg alloys is anodic dissolution assisted cracking [35, 39, 40, 51, 52]. SCC has been linked, to hydrogen uptake. For example, it has been reported that for 7xxx alloys, the initiation of SCC necessitates a critical concentration of hydrogen build up at potential crack sites [53]. More recently it has been documented that hydrogen plays a major role in the degradation of the mechanical properties, and is linked to embrittlement of 2024 alloy [9]. Studies of embrittlement of pure Al in humid air indicated a major role of hydrogen [54]. In particular, the intergranular crack path and the reversibility of the phenomenon (recovery of ductility after degassing) supported a hydrogen rather than an anodic dissolution mechanism. In a recent study [55], where glycerin was used as a non-corrosive environment, it was shown that Al-Zn-Mg-Cu-Zr alloy underwent hydrogen embrittlement even in laboratory air (having a relative humidity of ~50%). Similar trends were found in [56] after measurements of hydrogen permeability and stress corrosion resistance of a Al-Mg-Zn alloy, as functions of quench rate and aging treatment. Several research results have been reviewed in [4] for Al-Mg-Zn alloys. The kinetics of crack growth of aluminum alloy 7050 in a humid air environment was considered in [57], confirming that hydrogen embrittlement was the controlling mechanism. Evidence for hydrogen uptake and its effect to the crack growth for the low-strength alloy 5083 is summarized in [58].

## Accelerated corrosion tests

Accelerated laboratory tests do not precisely predict long-term corrosion behavior. However, they are frequently used when answers are needed quickly in the development of new materials. For this reason, accelerated tests are used to screen candidate alloys before conducting atmospheric exposures or other field tests. They are also sometimes used for quality control tests. Several new laboratory tests for exfoliation corrosion have been standardized in recent years under the jurisdiction of American Society for Testing and Materials (ASTM) Committee G- 1 on the corrosion of metals.

ASTM standard G 34 provides an accelerated exfoliation corrosion test for 2xxx and 7xxx alloys through the continuous immersion of test materials in an aqueous solution containing 4 M NaCl, 0.5 M potassium nitrate ($KNO_3$), and 0.1 M $HNO_3$ at 25°C. Susceptibility to exfoliation is determined by visual examination, using performance ratings established by reference standard photographs [59]. This method, known as the EXCO test, is primarily used in research and development and quality control of such mill products as sheet and plate. However, it should not be considered the optimal method for quality acceptance. Rather, this method provides a useful prediction of the exfoliation behavior of these alloys in various types of outdoor service, especially in marine and industrial environments. The test solution is very corrosive and is meant to represent the more severe type of environmental exposure.

It remains to be determined whether correlations can be established between EXCO test ratings and practical service conditions for given alloy. For example, it has been reported that samples of 7xxx alloys rated EA (superficial exfoliation) or P (pitting) in 48 h EXCO test did not develop more than superficial exfoliation (EA rating) during six to nine-year exposures to seacoast atmospheres, while materials rated as EC or E (severe and very severe exfoliation, respectively) developed severe exfoliation within or one to seven years at the seacoast.

## 2.3 Hydrogen damage in alloys

### General classification of hydrogen damage

Hydrogen damage is a form of environmentally assisted failure that results most often from the combined action of hydrogen penetration and residual or applied tensile stress. Hydrogen damage to specific alloys or groups of alloys manifests itself in many ways, such as cracking, blistering, hydride formation and loss in tensile ductility. For many years, these failures have been collectively termed hydrogen embrittlement and have been confused with other forms of environmentally induced failure; this term persists even though it is improperly used to describe a multitude of failure modes involving hydrogen, several of which do not demonstrate the classical features of embrittlement (that is reduced load carrying capability or fracture below the yield strength).

*Blistering* occurs predominantly in low-strength alloys when atomic hydrogen diffuses to internal defects, such as laminations or nonmetallic inclusions, and then precipitates as molecular hydrogen ($H_2$). The pressure of molecular hydrogen can attain such high values that localized plastic deformation of the alloy occurs, forming a blister that often ruptures. Blisters are frequently found in low-strength steels that have been exposed to aggressive corrosive environments (such as $H_2S$) or cleaned by pickling [60].

*Hydrogen environment embrittlement* occurs during the plastic deformation of alloys in contact with hydrogen bearing gases or a corrosion reaction and is therefore strain rate dependent. The degradation of the mechanical properties of ferritic steels, nickel-base alloys, titanium alloys, and metastable austenitic stainless steels is greatest when the strain rate is low and the hydrogen pressure and purity are high.

*Hydrogen stress cracking* often referred to as hydrogen-induced cracking or static fatigue is characterized by the brittle fracture of a normally ductile alloy under sustained load in the presence of hydrogen. Most often, fracture occurs at sustained loads below the yield strength of the material. Hydrogen stress cracking is associated with absorption of hydrogen and a delayed time to failure (incubation time) during which hydrogen diffuses into regions of high triaxial stress.

*Hydrogen attack* is a high-temperature form of hydrogen damage that occurs in carbon and low-alloy steels exposed to high pressure hydrogen at high temperatures for extended time. Hydrogen enters the steel and reacts with carbon either in solution or as carbides to form methane gas, which may result in the formation of cracks and fissures or may simply decarburize the steel resulting in a loss

in strength of the alloy. This form of damage is temperature dependent, with a threshold temperature of approximately 200 °C [61, 62].

*Loss in tensile ductility* was one of the earliest recognized forms of hydrogen damage. Significant decreases in elongation and reduction in area are observed for steels, stainless steels, nickel-base alloys, aluminum alloys, and titanium alloys exposed to hydrogen. This mode of failure is most often observed in lower-strength alloys, and the extent of loss in tensile ductility is a function of hydrogen content of the material. Loss in tensile ductility behavior is strain rate sensitive and becomes more pronounced as the strain rate decreases [63].

*Degradation in flow properties* in hydrogen environments has been found at ambient temperatures for iron and steel and at elevated temperature for several alloy systems. The steady-state creep rate under constant load has been observed to increase in the presence of hydrogen for some nickel-base alloys.

*Hydride formation* produces embrittlement in magnesium, tantalum, niobium, vanadium, uranium, thorium, zirconium, titanium, and their alloys, as well as many other less common metals and alloys. The degradation of mechanical properties and the cracking of these metals and their alloys are attributable to the precipitation of metal hydride phases. Hydrogen pickup often results from welding, heat treating, charging from a corrosion process, or during melting of the alloy.

## Corrosion- induced hydrogen embrittlement in aluminum alloys

Although over the last fifty years extensive research has been focused on hydrogen embrittlement of aluminum alloys, there is still much debate on the prevailing mechanisms involved. Hydrogen enhanced localized plasticity (also known as HELP), hydride formation, and hydrogen enhanced decohesion (HEDE) are among the mechanisms proposed. The bulk of research results deal with 7xxx alloys, while work on 2xxx alloys is rather limited.

The HELP mechanism was introduced in the early 70's to explain the hydrogen embrittlement in steels. It is based on the observations that hydrogen diffusing in front of a crack tip and through the material lattice actually enhances dislocation movement rather than hindering it [64]. The theory was adopted for BCC and FCC crystal structures [65-67]. With in situ TEM observation of the fracture process in real time, with vacuum or $H_2$ atmospheres, it was observed that hydrogen increased the dislocation mobility under constant stress, while the reverse effect was true with the removal of hydrogen and restoration of vacuum. Similar observations and conclusions were reached for pure aluminum [68]. Studies, using the Peierls–Nabarro model of dislocation stress fields, were performed in Al, to study the interaction of interstitial hydrogen with dislocations. Hydrogen was found to form a strong bond at dislocation cores, depending on the type of dislocation and that it lowered the Peierls stress of dislocations by more than an order of magnitude [69].

The HEDE mechanism works under the same initial assumptions as the HELP mechanism described above. Through interaction between the corrosive media and the material surface, atomic hydrogen forms and is subsequently absorbed in the material. Then it diffuses in the areas in front of crack tips,

which are characterized by high triaxiality. According to the HEDE mechanism, hydrogen in these regions leads to a loss in the cohesive strength, thus enabling crack advance [70].

Hydride formation of either Al [71] or microstructural phases other than aluminum (e.g., Mg or Li-containing phases) has been detected in a few studies [72, 73]. The implicit assumption is that hydrides are brittle phases with limited fracture toughness and very low fracture strength, being only a small fraction of the theoretical fracture strength of Al. Thus formation of hydrides of continuous secondary phases at key locations, such as along grain boundaries, provides an alternative mechanism for embrittlement in aluminum alloys.

## 2.4 Induced hydrogen evolution and trapping

During corrosion hydrogen evolution can take place in an aqueous acidic solution by the cathodic reaction

$$2H^+ + 2e^- \rightarrow H_2$$
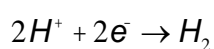
In a $H_2O$ rich environment and with the possible presence of $Cl^-$ anions, hydrogen is produced by corrosion reactions at the surface of the material and part of it is absorbed into the material [74]. In particular, the process of atomic hydrogen production by a single-electron transfer, according to the reaction

$$H_2O + e^- \rightarrow OH^- + H$$
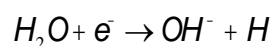
makes water an aggressive environment for aluminum alloys [57]. Absorbed hydrogen diffuses towards the interior of the material and may be trapped at various preferential locations. It has been shown [75, 76] that lattice defects (vacancies, dislocations, grain boundaries) and precipitates supply a variety of trapping sites. Hydrogen traps are mechanistically classified as reversible and irreversible [77], depending on the steepness of the energy barrier needed to be overcome by hydrogen to escape from them. These traps can be thermally activated and liberate hydrogen at different temperatures.

In order to investigate hydrogen uptake and trapping, a variety of methods to introduce hydrogen in the microstructure have been used over the years, such as exposure to aqueous environments and humid air [78], cathodic charging [79] as well as exposure to a corrosive environment.

Thermal desorption spectroscopy (TDS) along with permeation techniques are the most well established methods for determining hydrogen uptake. Permeation gives information about the diffusivity of hydrogen through the bulk of the material, but does not distinguish between the active trapping sites present in the alloy microstructure. This information can be obtained by thermal desorption methods combined with gas chromatography or mass spectroscopy. The setup consists of a furnace with a system of automatic temperature control, a supply of inert gas (high-purity nitrogen) and a gas chromatograph.

This approach has been successfully adapted to the studies of hydrogen trapping in various materials with BCC and FCC structure [9, 80-82] as in nickel [80, 83], pure aluminum [82, 84, 85], Al-Cu, Al-

$Mg_2Si$ [75], Al-Li alloys [85, 86], Al-Li-Cu-Zr [87], as well as pure iron and steel [88-90]. It has also been combined with accelerated corrosion tests in order to characterize corrosion and hydrogen absorption in alloy 2024 [45, 46]. In the last two works, the existence of multiple trapping states was confirmed and the quantity and evolution pattern of hydrogen was discussed.

TDS measurements have been combined with heat treatments for second-phase precipitation or dissolution, as well as cold working for dislocation multiplication in order to determine the constitution of trapping sites in nickel, steel, pure aluminum as well as Al alloys [75, 82, 91-93]. Hydrogen uptake and trap binding energy were determined for Monel K-500 in several conditions (solid solution, aged and cold worked microstructures), using TDS [94]. The results suggested hydrogen trapping at incoherent γ′ ($Ni_3Al$) precipitates. Transport and trapping of hydrogen in nickel has been investigated in [92]. It was shown that dislocations in nickel act as trapping places of hydrogen, and the activation energy of these traps seem to be lower than the activation energy for the bulk diffusion of hydrogen. It was proposed, that in nickel hydrogen diffuses along short-circuit routes through the grain boundaries but hydrogen is also trapped at grain boundaries. The effect of grain size on hydrogen diffusion and trapping mechanisms has been investigated for a wide range of grain sizes in nontextured pure nickel in [80]. The conclusion was reached that hydrogen diffusion is intensified along the boundaries but may decrease when the dislocation density stored in the boundary becomes considerable [80, 83].

Regarding hydrogen trapping in aluminum alloys, thermal desorption spectroscopy has been performed in pure aluminum in [82]. The desorption spectra revealed three distinct trapping states. The lowest energy peak was attributed to hydrogen occupying interstitial lattice sites. The intermediate peak around 400$^o$C was associated with hydrogen trapped at dislocations, while the 500$^o$C trap state with vacancies. Relevant work in [84], investigated hydrogen trapping states in pure aluminum foils of 99.99% purity with different amount of blisters by means of TDS. Blisters as well as vacancies have been recognized as potential sites of hydrogen trapping. More specifically in aluminum alloys, it has been shown in [75, 76] that lattice defects (vacancies, dislocations, grain boundaries, subgrain boundaries, interfaces), second-phase particles and precipitates supply a variety of trapping sites. Tritium microautoradiography was employed to study hydrogen trapping in high purity aluminum, Al-4Cu, Al-$Mg_2Si$ and Al-6Zn-2Mg (wt.%) alloys in [75] and [95]. These works indicated that, in general, microstructural features possessing a tensile stress field act as hydrogen traps while those having a compressive stress field act as hydrogen repellers. In some alloys, trapping was observed at dislocations produced by cold work and at interfacial dislocations associated with tensile elastic stress fields. The effect of hydrogen on the hardness of 7075-T6 aluminum alloy has been investigated in [96]. The surface of 7075-T6 aluminum alloy was hardened by the introduction of hydrogen. Further charging increased the depth of the hardened region. Transmission electron microscopy observations of the hardened hydrogen-enriched layer revealed an increase in dislocation density. Aging after hydrogen charging had as a result either the complete or partial recovery of hardness depending on the charging conditions applied to the material. Hydrogen

enrichment was also determined in a 2050 Al-alloy subjected to cyclic corrosion tests in aqueous NaCl solutions [97].

Corrosion–induced hydrogen uptake and subsequent trapping has been extensively investigated in [9, 11, 45, 46]. 2024-T351 alloy has been subjected to accelerated corrosion by immersion in EXCO solution specified in ASTM G34-90 [59]. Hydrogen is introduced by the cathodic hydrogen reaction. Hydrogen uptake and trapping were studied by TDS, using the system previously mentioned. The peaks correspond to respective trapping states. Four traps T1, T2, T3 and T4 were highlighted. The last three traps are irreversible since no hydrogen evolves below the respective critical temperature. The first trap T1 is a reversible trap due to the fact that it releases hydrogen continuously at temperatures close to ambient temperatures. Calculation of the total hydrogen quantity liberated from each trapping site is given by integrating the area under the respective peak given by spectrum of TDS method. The three irreversible traps exhibit saturation, indicating depletion of the available trapping sites. Trap T4 is the first to saturate and exhibits the highest desorption temperature. It is therefore considered as the strongest trap.

The hydrogen spectrum provides some clues about trapping states, based on the temperatures where hydrogen evolution takes place. During the thermal cycle of TDS the material undergoes microstructural changes. A comparison between the hardness of corroded versus uncorroded material that undergoes the same thermal cycle, proves that the hardness of uncorroded material declines with temperature up to 400°C due to overaging, while it rises again above 400°C due to dissolution and re-precipitation. A similar behavior is exhibited by the corroded material. However there are two distinct differences in the hardness values. The corroded material is softer than the uncorroded up to 300°C and harder above 350°C. The first temperature region includes T1 and T2 states. Hydrogen in the T1 state is trapped in interstitial sites while T2 hydrogen is trapped at particle/matrix interfaces.

Recently it was suggested that hydrogen might assist dislocation motion by altering the binding energy between dislocations and solute atoms [98, 99]. On the other hand, hydrogen at matrix/particle interfaces might alter the interaction energy between dislocations and particles for coherency hardening in a way similar to that proposed for lattice dislocation. The result is that hydrogen in T1 and T2 states most likely aid dislocation motion in overcoming either the lattice resistance or semicoherent particle resistance and the corroded material appears softer. The second temperature region (above 300°C) incorporates states T3 and T4. It is presently argued that T3 hydrogen is trapped at dislocations, while T4 hydrogen is trapped in the main hardening phase S-$CuMgAl_2$. Hydrogen affects the dissolution and re-precipitation process or even the overaging (coarsening) process in the alloy and the corroded alloy appears harder.

In an attempt to gain a better insight of hydrogen trapping in aluminum alloy 2024 experiments were designed to alter the materials microstructure prior to corrosion exposure and associated hydrogen uptake. Details regarding the experimental procedures are described in [11]. Due to the short corrosion exposure times, the hydrogen produced by the corrosion process is not enough to reveal

all trapping states identified in [9] and, therefore, only the strong trap state T4 appears. Comparison of the SQ and SQA curves shows a marked decrease in the amount of hydrogen trapped in the T4 state for the SQ series. This result suggests that T4 state is mainly associated with the S-phase (Al2CuMg) since this phase is absent in the SQ specimen. Furthermore it has been indicated with atom probe tomography, that the S-phase acts as hydrogen trap in AA2024 alloy [100]. The onset of hydrogen desorption for the SQ series is displaced to higher temperatures relative to the SQA series. This suggests that, in the absence of the S-phase, hydrogen is being trapped in a stronger trap site in the SQ specimens. This trap should be associated with vacancies that were thermally formed during the solution treatment of the SQ-specimens. These vacancies were frozen-in after the quench and acted as hydrogen trap sites during the corrosion exposure. Hydrogen trapping in vacancies has been also documented in pure aluminum, where the vacancies constitute the strongest trap state with desorption temperature at about 500°C [79, 82].

# Chapter 3 – Experimental procedures

## 3.1 Material Studied

As stated earlier, the main focus of this research was aluminum alloys belonging to the 2xxx alloy series, more accurately, alloy 2024. The material was obtained in plate form, that had not been anodized and its only surface protection emanated from the thin protective oxide, which is created when the material is exposed to atmospheric air. Material was obtained from several suppliers and with thickness 3.2mm.

The chemical composition of the material is displayed below in Table 3. 1 and below in Table 3. 2 the thermal treatments of the alloys are presented.

Table 3. 1: Chemical composition of alloys of aluminum (%wt.).

| Sample | Al | Si | Fe | Cu | Mn | Mg | Cr | Zn | Ti | Other |
|--------|------|------|------|------|------|------|------|------|------|-------|
| 2024 | 90,7-94 | 0,50% | 0,50% | 4,35% | 0,60% | 1,5% | 0,10% | 0,25% | 0,15% | 0,15% |

Table 3. 2: Thermal treatments of aluminum alloys.

| Material | Temperature Dissolution | Quenching | Cold rolling | Thermal treatment |
|----------|------------------------|-----------|--------------|-------------------|
| 2024 Bare | 495 °C | 0°C | No | Aging 170°C<br><br>Aging 210°C |

The labeling scheme used to identify the orientations and planes of the alloys is shown in Fig. 3. 1.
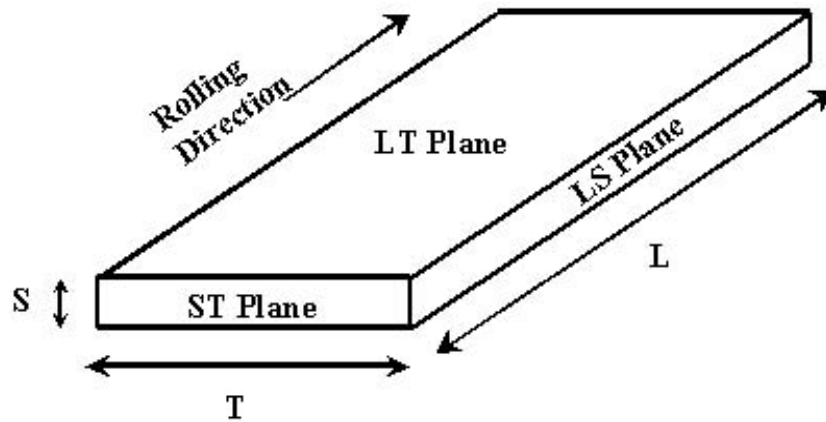


Fig. 3. 1: Labelling scheme used for directions and planes.

## 3.2 Microstructural characterization

All specimens were prepared using classical metallographic techniques. The non-corroded specimens were cut from the plate of the corresponding material with the use of a microtome (Struers Accutom).The specimens for metallographic observation were placed in simple epoxy resin (Acryfix) that stabilizes in atmospheric temperature (20-25$^0$C) in roughly 10 minutes.

The specimens were placed in epoxy resin for easy handling. The resin fills the pores, voids and surface abnormalities of the specimen. This process is essential for the maintenance of pits and microcracks during the next steps of preparation. The surface planes under observation were the rolling surface and the side surface (LT and LS plane in Fig. 3. 1. Next the specimens were initially grinded on SiC abrasive wheels. The sizes of grains were 80, 220, 500, 800, 1000, 2000 grid. Polishing of the specimens followed on special disks with diamond paste of 3μm and 1μm grain size respectively. The last stage of preparation was polishing with $Al_2O_3$ particles of 0,3μm and 0,05 diameter respectively. Finally the surface was chemically etched with Keller's reagent. This reagent has a chemical composition of: *2,5 ml HNO₃, 1,5 ml HCl, 1,0 ml HF and 95,0 ml H₂O*. The time of exposure in Keller's was a few seconds. Finally the specimens were washed with distilled water and alcohol and dried in a purge of warm air [101].

## 3.3 Accelerated corrosion testing

Accelerated corrosion testing that provides a useful simulation of the exfoliation behavior of these alloys in various types of outdoor service, especially in marine and industrial environments, was employed. The accelerated corrosion test (EXCO) is described in ASTM specification G34-90 [59]. It includes exposure at 22°C, for 4 hours, for the not-heat treated specimen, in a solution containing 234g NaCl, 50g $KNO_3$ and 6,3ml concentrated $HNO_3$ (70%wt) diluted to 1 L of distilled water. The quantity of solution used is proportional to the specimen external surface area, with the minimum amount required being 10 ml for every $cm^2$ of specimen surface and the maximum 30ml. Specimen cleaning, after removal from the corrosive solution involved soaking in concentrated $HNO_3$ (70%wt) for 5 minutes, rinsing in distilled water, then in acetone and thoroughly drying in a purge of warm air. The entire cleaning process should not exceed 10 minutes. Then, half of the specimens were placed in simple epoxy resin for metallographic observation and others were used for the determination of hydrogen quantity trapped in the material's microstructure.

## 3.4 Heat treatment

Some specimens were surface-cleaned with alcohol according to ASTM G1 and then were heat treated. The specimens all artificially aged, after solid solution at 495°C for 30 minutes. Different artificial aging conditions were performed for the specimens at 170°C and 210°C respectively, in an electric oven with ±4 °C temperature control and for different aging times.

The aging temperatures were selected in order to affirm the results of the artificial aging of the commercial sheet AA2024-T3, according to a paper by Alexopoulos et al. [102]. Aging times were selected to correspond to all aging conditions, including Under-Aging (UA), Peak-Aging (PA) and Over-Aging (OA). All of the available specimens were exposed for 4 hours to the laboratory exfoliation corrosion (EXCO solution) according to specification ASTM G34. Then, half of the specimens were placed in simple epoxy resin for metallographic observation and others were used for the determination of hydrogen quantity trapped in the material's microstructure.

## 3.5 Hydrogen measurements

A main part of this thesis consists of the determination of hydrogen concentration and it's trapping states in the material after corrosion. The determination of these states was conducted by using a thermal desorption technique.

The scope of this process was to measure the amount of hydrogen eluting from specimens previously subjected to various periods of exfoliation corrosion exposure as a function of temperature. Strips of

the materials, 3.2mm wide and 20 mm long, were be cut at right angles to the rolling direction and were exposed to exfoliation corrosion. The large surface to volume ratio of the specimen was chosen with a view to decreasing the hydrogen evolution time and increasing the sensitivity of the measurements. The exfoliation accelerated corrosion test is described in ASTM specification G34-90 as is mentioned above in 3.2. Hydrogen evolved from the corroded specimen with controlled heating in an inert atmosphere and was measured using a gas chromatograph.

For the determination of hydrogen quantity trapped in the material's microstructure an in-house experimental setup was used. This setup consists of a furnace with a system of automatic temperature control, a supply of inert gas (high-purity nitrogen) and a gas chromatograph equipped with a valve for sampling gases. The sample was placed in a 10 mm diameter quartz tube and held in place by an inert porous diaphragm, permeable to the gas (quartz wool). The tube was inserted in the furnace and subjected throughout the experiment to a flow of **Q=30ml/min** high purity nitrogen. This flow was then driven to a gas chromatograph equated with a TCD detector. Calibration runs were performed using standard $H_2 - N_2$ mixtures, of volume concentration 1000 and 10000 ppm. Blind experiments were conducted with an empty tube heated up to 600$^o$C and no hydrogen was detected. The temperature of furnace was increased at a rate of approximately 5$^o$ C/min and the nitrogen current swept along everything that was emitted by the sample and carried it in the gas chromatograph. The sampling was performed manually through the gas-sampling valve about every 2 minutes.

Primary data consist of curves of the intensity, I, of TCD detector signal (in μV) versus time, combined with the temperature history of the specimen. Detector intensity is converted to hydrogen mass flow rate, m, by the expression

$$m=\alpha I Q$$

where α has units of g of $H_2$/(ml μV). It is the calibration constant of the detector expressing the mass concentration of hydrogen per μV indication of the detector. During the present work, a small deterioration of the accuracy of the detector was witness, which was taken into account in the data.

The results reported in the next section are presented as hydrogen mass flow rate (in μg/min) versus specimen temperature. If the heating rate is sufficiently low, each trapping site produces an independent peak. The temperature of the onset of peak growth is characteristic of the energy needed to release hydrogen from the respective trapping site. Thus, low temperature peaks are related to weakly bonded hydrogen and high temperature peaks to strongly bonded hydrogen. Calculation of the total hydrogen quantity in each trapping site is performed by integrating the area under the respective peak.

# Chapter 4 – Results and Discussion

## 4.1 Metallography – Microstructural Characterization

### Objectives

The objectives of the microstructural characterization are the following:

- To evaluate possible differences in the microstructure between the as received materials and the artificially aged.
- To assess the corrosion damage in terms of pitting, intergranular corrosion, exfoliation corrosion and depth of attack for the material after artificial aging
- To determine possible pathways of hydrogen trapping/entry in the material during corrosion.

As explained in the preceding chapter, optical microscopy characterization technique was used in order to assess corrosion damage at microstructural level. Intergranular corrosion, exfoliation attack and hydrogen pathways were assessed with metallographic sectioning.

The as received material was prepared for metallographic observations, as described in Chapter 3. The resulting microstructure is presented in Figures Fig.4.1- Fig.4.3. Fig.4.1 depicts metallographic images in the LS direction for magnifications x100, x200 and x500 respectively. It is observed, that in the longitudinal direction, the grains are elongated and several second phase particles appear along the grain boundaries.
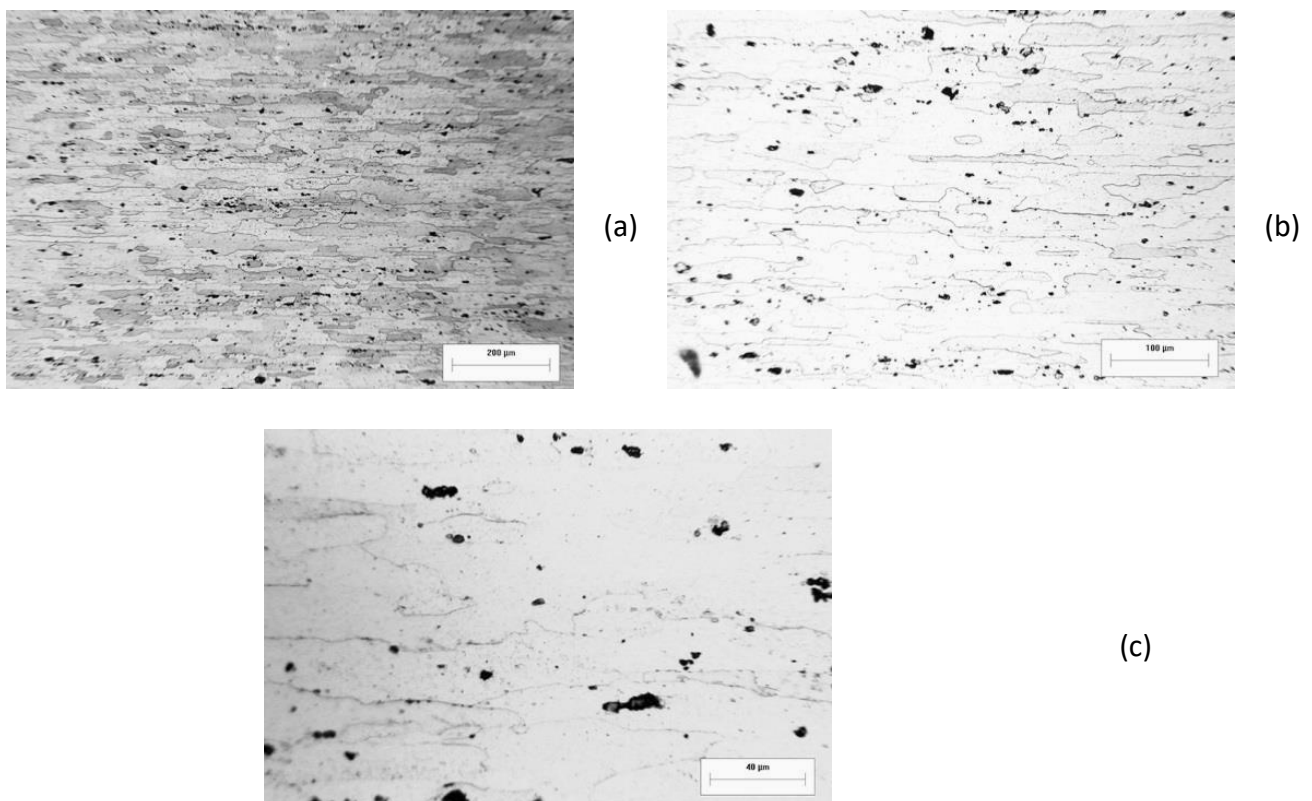

(a)


(b)


(c)

Fig.4.1: As received aluminum alloy 2024-T351. Metallographic images in the longitudinal direction (LS plane) for magnifications (a) x100, (b) x200 and (c) x500 respectively.

Figure 4.2 depicts metallographic images on the LT (rolling) plane for magnifications x100, x200 and x500 respectively. Second phase particles are observed along the grain boundaries.
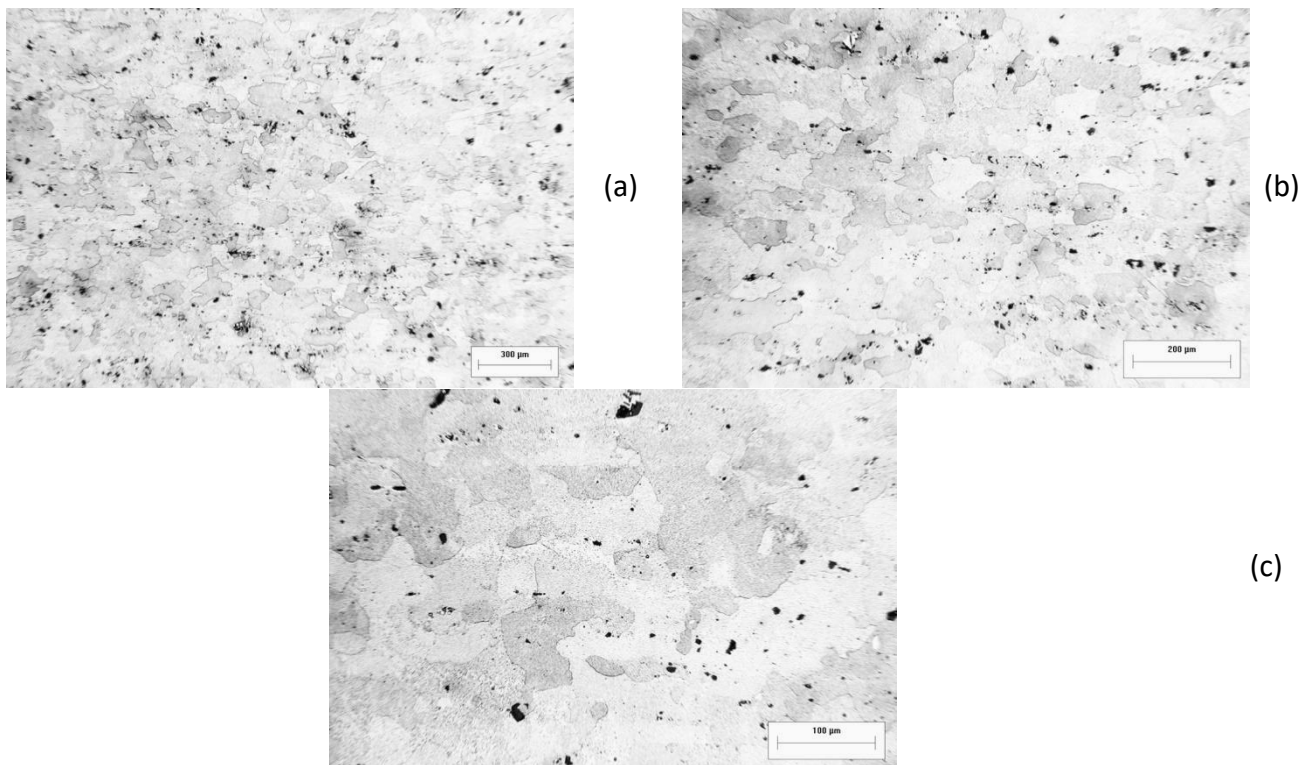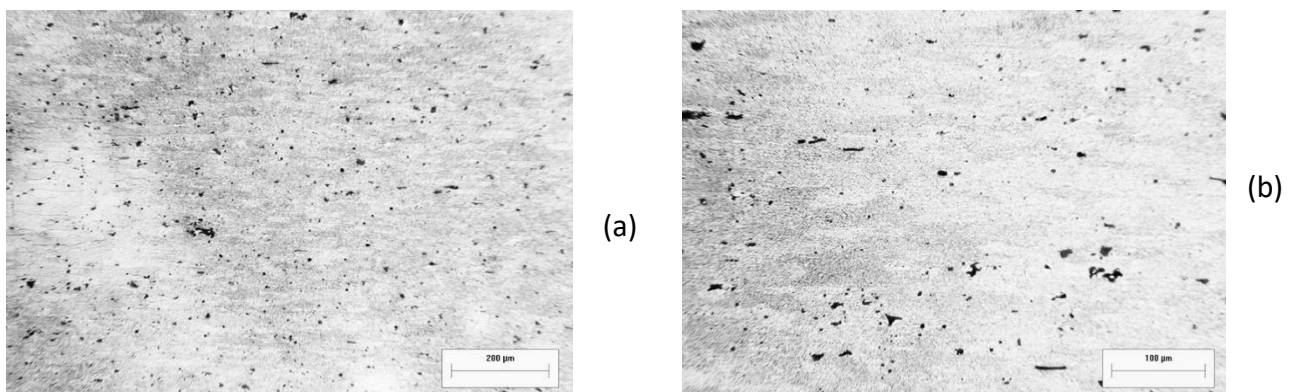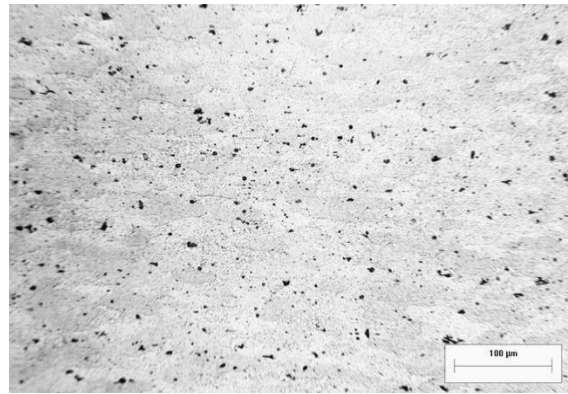






Fig.4.2: As received aluminum alloy 2024-T351. Metallographic images from the surface of the specimen (LT plane) for magnifications (a) x50, (b) x100, (c) x200 respectively.

Fig.4.3 depicts metallographic images in the transverse (ST) direction for magnifications x100, and x200. Similarly, it is observed, that along this direction the grains are elongated and several second phase particles appear along the grain boundaries.
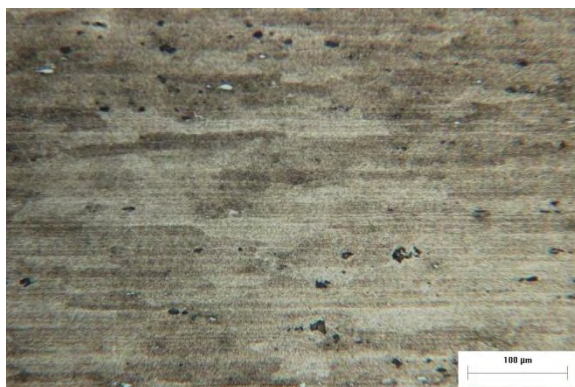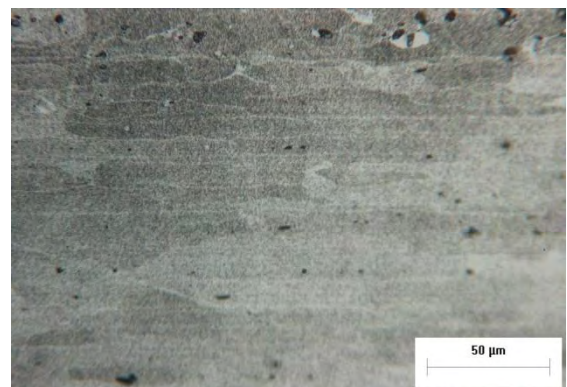
(c)

Fig.4.3: As received aluminum alloy 2024-T351. Metallographic images in the transverse direction (ST plane) for magnifications (a) x100, (b) x200 and(c) x200 respectively.

Metallographic characterization of the material after aging at 210°C, for varying aging times was conducted. The following figures depict metallographic images of the heat treated specimens. All metallographies were acquired on the LS plane. Specimen with aging time 30 minutes is depicted in figure 4. 4. The surface appears over etched in comparison with the as received material and the grain boundaries are indicated as white areas. The etching technique used was the same as in the case of the as received material. In figures 4.5, 4.6 and 4.7 the specimens were aged for 6, 15 and 54 hours respectively and the grain boundaries exhibit similar characteristics as in figure 4.4. The interior of the grains is dark and the grain boundaries white, this is an indication that during aging at 210°C, the temperature is high enough so that the grain boundaries are depleted by the solute which migrates in the grain interior and forms larger S phase particles.
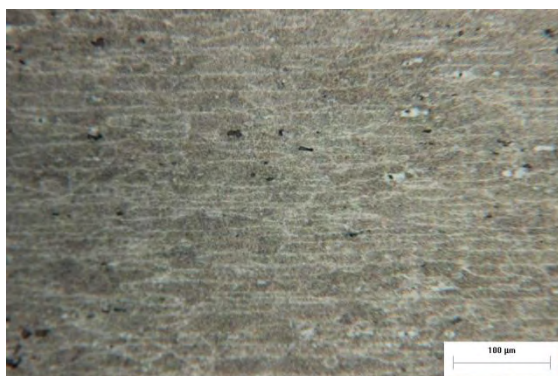


(a)



(b)
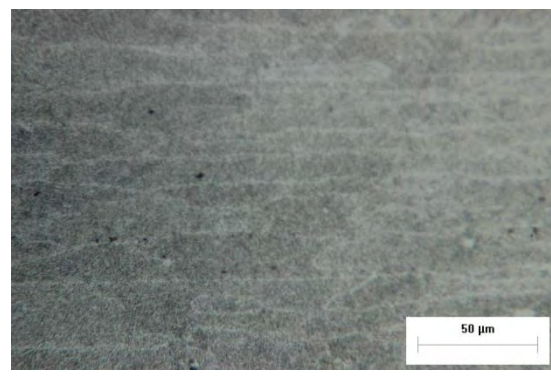
Fig.4.4:Heat treated aluminum alloy 2024-T351 for 30 mins at 210°C. Metallographic images in the longitudinal direction (LS plane) for magnifications (a) x200 and (b) x500 respectively.



(a)



(b)

Fig.4.5:Heat treated aluminum alloy 2024-T351 for 6 hours at 210°C. Metallographic images in the longitudinal direction (LS plane) for magnifications (a) x100, (b) x200 and (c) x500 respectively.
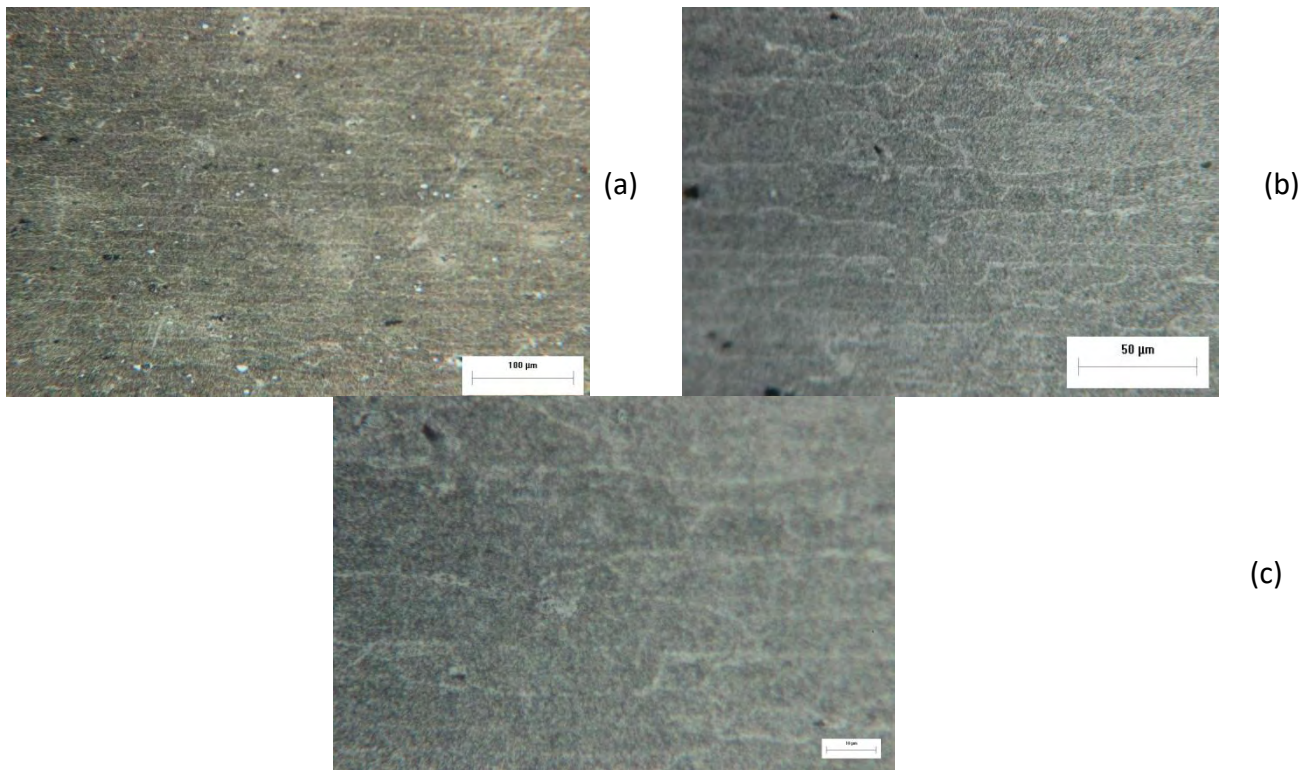
Fig.4.6:Heat treated aluminum alloy 2024-T351 for 15 hours at 210°C. Metallographic images in the longitudinal direction (LS plane) for magnifications (a) x200, (b) x500 and (c) x1000 respectively.



Fig.4.7:Heat treated aluminum alloy 2024-T351 for 54 hours at 210°C. Metallographic images in the longitudinal direction (LS plane) for magnifications (a) x200 and (b) x500 respectively.

## 4.2 Accelerated corrosion testing of the heat treated material

The experimental procedure involves the following actions:

1) Accelerated corrosion testing(using the EXCO procedure)
2) Detailed microstructural investigation of the evolution of corrosion damage by employing metallography.

All specimens were prepared using classical metallographic techniques.

## Effect of aging on the microstructural assessment of exfoliation corrosion

Available specimens were surface cleaned with alcohol according to ASTM G1 and then were heat treated. The specimens all artificially aged, after solid solution at 495°C for **30 minutes**. The specimens were artificially aged at **210°C**, in an electric oven with ±4°C temperature control. This aging temperature was selected to affirm the results of the artificial aging of the commercial sheet AA2024-T3,according to [102]. Aging times were selected to correspond to all aging conditions, including Under-Aging (UA), Peak-Aging (PA) and Over-Aging (OA). Specifically the different artificial aging conditions, where these specimens were performed, were respectively 30 min, 1 h, 2 h, 4h, 6 h, 9 h, 15 h, 24 h, 36 h, 48 h, 54 h and 63 h.

All the available specimens were exposed for 4 hours to the laboratory exfoliation corrosion (EXCO solution) according to specification ASTM G34. Then, the specimens were placed in simple epoxy resin for metallographic observation. Metallographic sections were also prepared and examined in order to determine the depth of attack versus aging exposure time at standard temperature conditions, as well as the pathways of corrosion progression. Figures 4.8 to 4.14 depict the progression of exfoliation corrosion for 30min, 6 hours, 9 hours, 24 hours 48 and 54 hours. The intergranural nature of corrosion is apparent from the on start of the corrosion process at 30 min after 6 hours it has already progressed to exfoliation corrosion. The exfoliation process becomes more intense with the increase in aging time. Corrosion starts in the form of isolated pits. In the first 30 min of exposure pits deepen and grow laterally. Pit density increases and pit-to-pit interaction starts. Pits interact via intergranular corrosion .This leads to pit coalescence and pit cluster formation. Pit clusters grow laterally beneath the material surface via intergranular corrosion, leading to exfoliation of surface layers of the material. This type of damage evolution, more specifically the intergranular network supporting pit growth is also responsible for the transport of corrosion solution deep in the material, so that the corrosion reaction takes place in a certain depth producing hydrogen. This is one of the main mechanisms of hydrogen transport in relatively high depths, which cannot otherwise be explained solely by diffusion from the material surface. However once hydrogen is produced, e.g. at the bottom of a corrosion pit, it diffuses to the adjacent unaffected material and establishes a hydrogen diffusion zone below the corrosion zone.

### *Aging time 30 mins*



(a)



(b)

(c)

Fig.4.8:Corroded aluminum alloy 2024-T351 after aging for 30 mins at 210°C. Metallographic images in the longitudinal direction (LS plane) for magnifications (a) x200, (b) x500 and(c) x500 respectively.
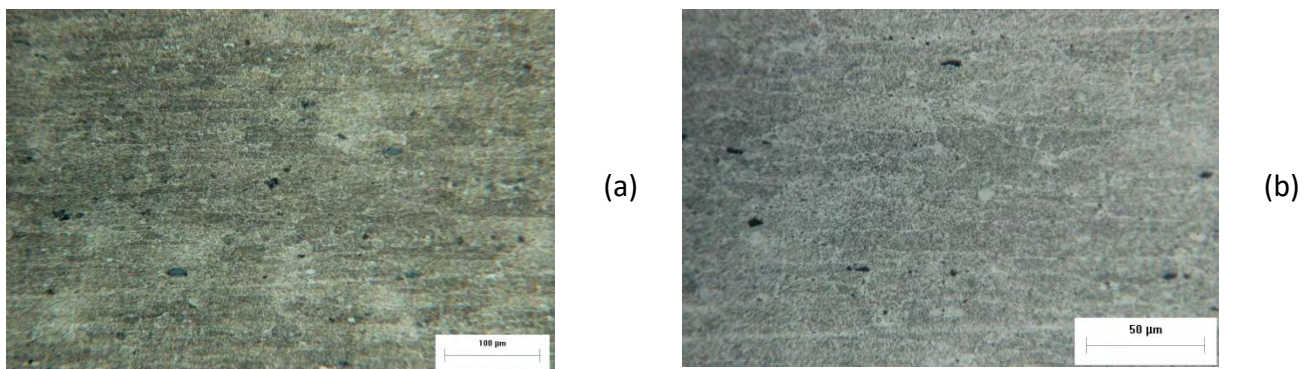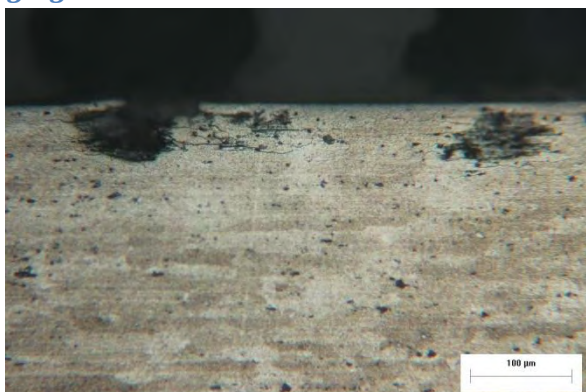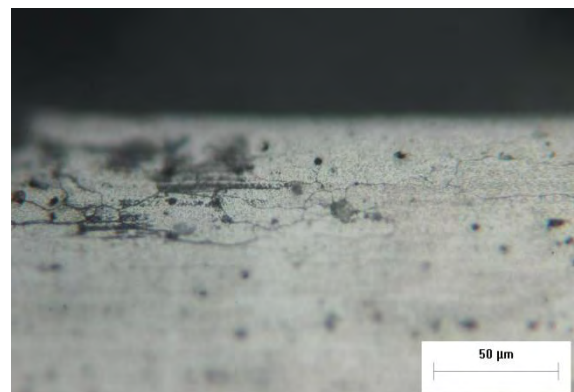
*Aging time 6 hours*



(a)



(b)



(c)

Fig.4.9:Corroded aluminum alloy 2024-T351 after aging for 6 hours at 210°C. Metallographic images in the longitudinal direction (LS plane) for magnifications (a) x100, (b) x200 and(c) x500 respectively.
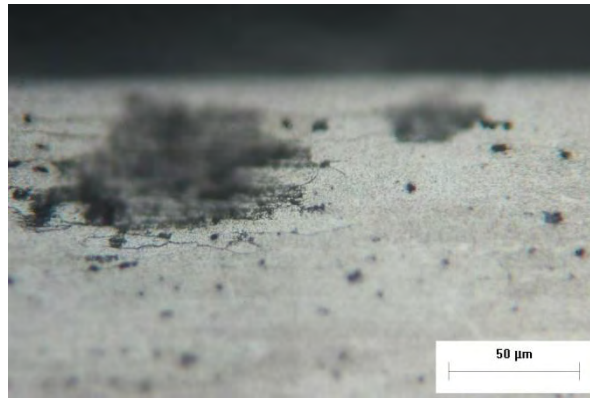
*Aging time 9 hours*



(a)



(b)

Fig.4.10:Corroded aluminum alloy 2024-T351 after aging for 9 hours at 210ºC. Metallographic images in the longitudinal direction (LS plane) for magnifications (a) x100, (b) x200 respectively.
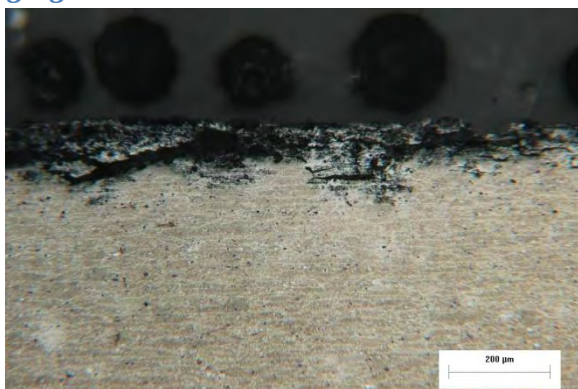
*Aging time 15 hours*



(a)

(b)

(c)

Fig.4.11:Corroded aluminum alloy 2024-T351 after aging for 15 hours at 210ºC. Metallographic images in the longitudinal direction (LS plane) for magnifications (a) x100, (b) x200 and(c) x500 respectively.

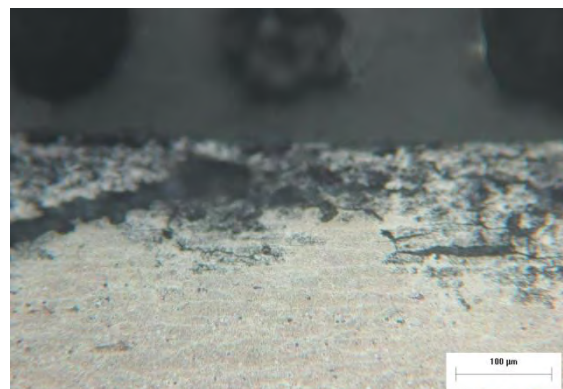*Aging time 24 hours*



(a)

(b)

(c)

Fig.4.12:Corroded aluminum alloy 2024-T351 after aging for 24 hours at 210°C. Metallographic images in the longitudinal direction (LS plane) for magnifications (a) x100, (b) x200 and(c) x500 respectively.
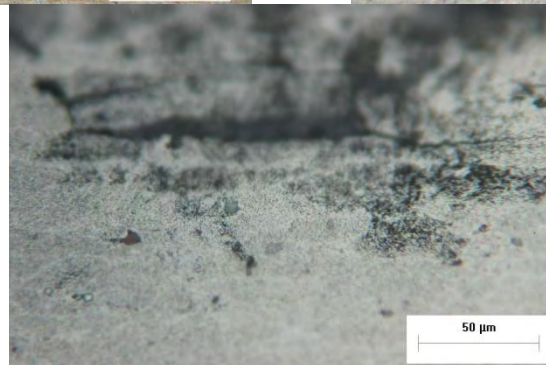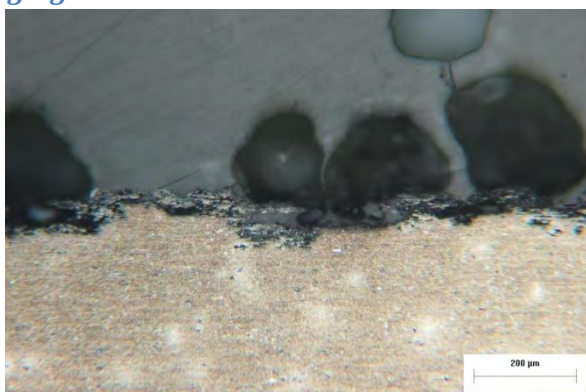
*Aging time 48 hours*
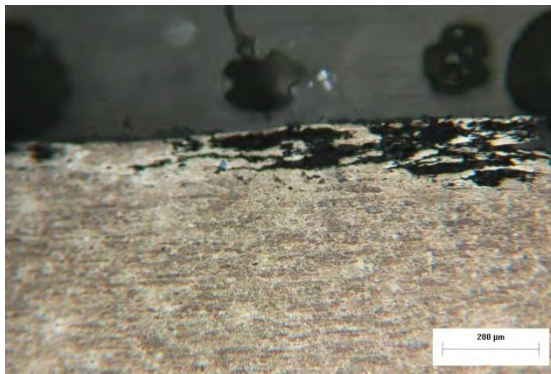


(a)
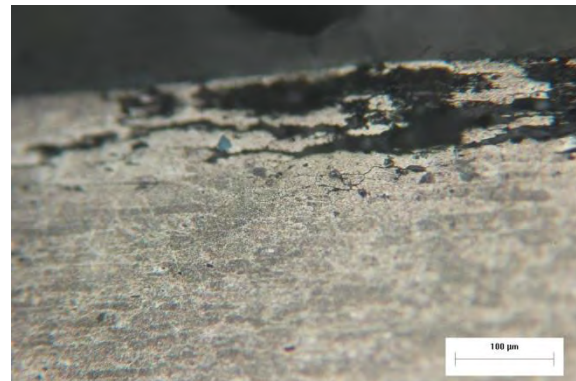


(b)
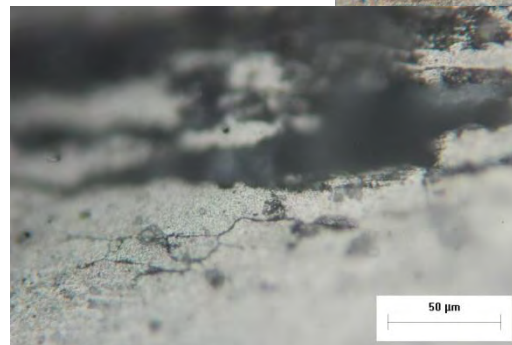


(c)

Fig.4.13:Corroded aluminum alloy 2024-T351 after aging for 48 hours at 210°C. Metallographic images in the longitudinal direction (LS plane) for magnifications (a) x100, (b) x200 and(c) x500 respectively.
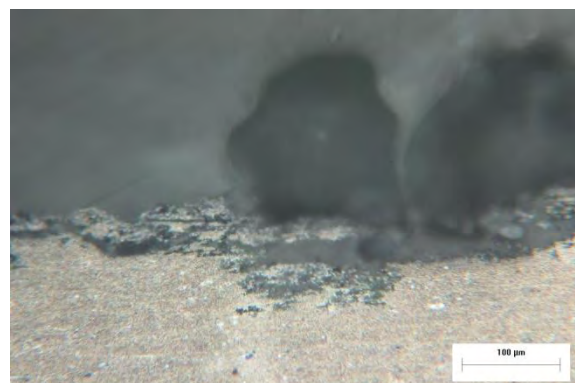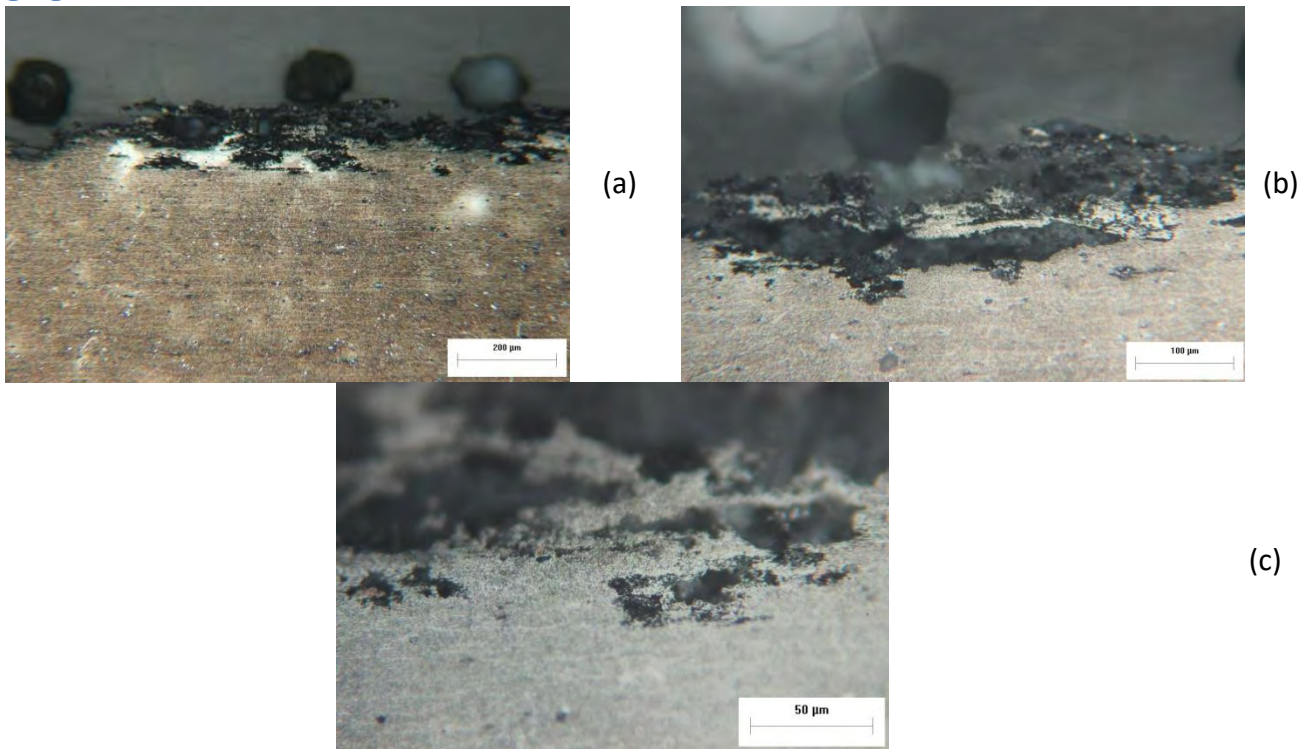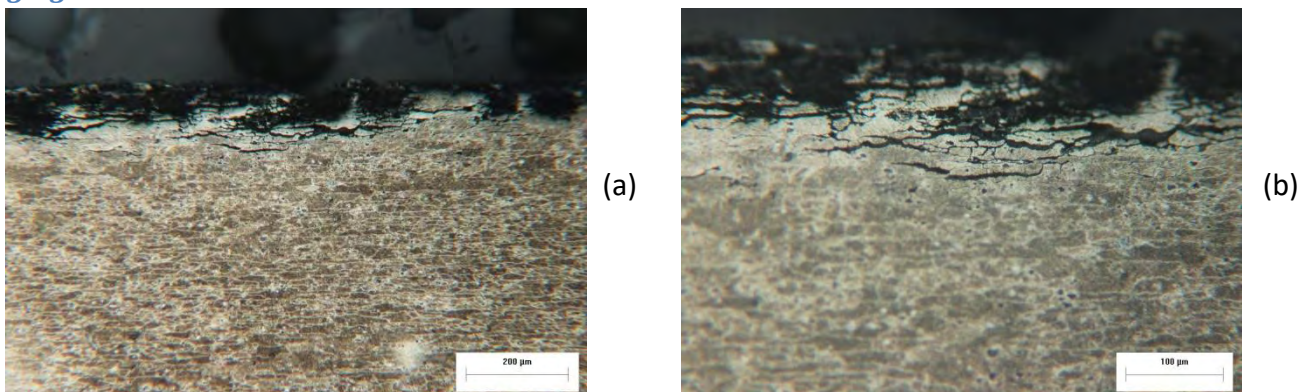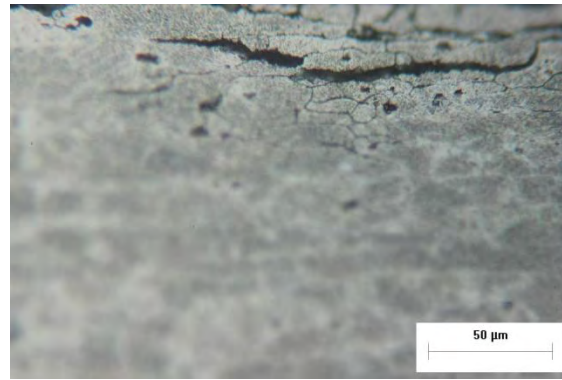
*Aging time 54 hours*
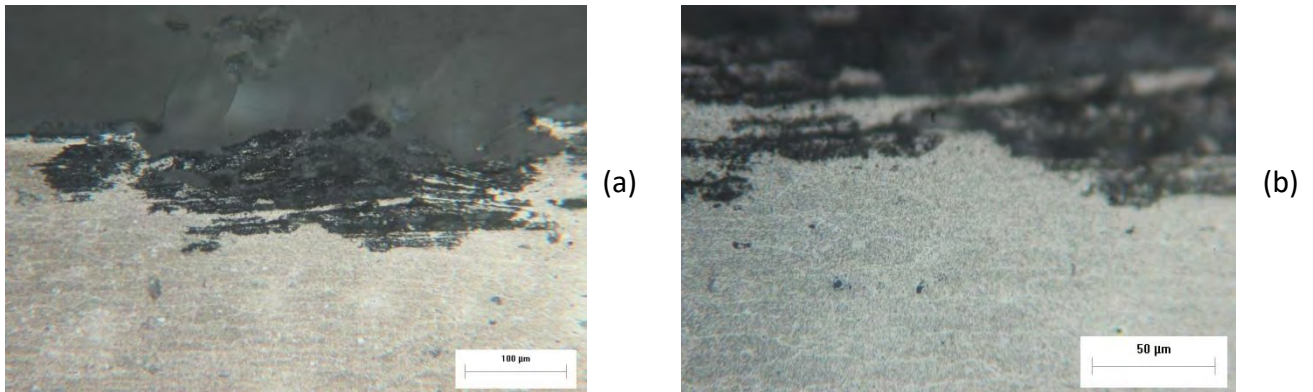


Fig.4.14:Corroded aluminum alloy 2024-T351 after aging for 48 hours at 210ºC. Metallographic images in the longitudinal direction (LS plane) for magnifications (a) x200 and (b) x500 respectively.

## Effect of aging on the exfoliation corrosion depth of attack

Metallographic section where the depth of attack was measured, were also performed in order to evaluate the evolution of corrosion damage with respect to exposure time.

*Aging time 30 min*

Initially, several of the aluminum alloy 2024-T351 specimens, were artificially aged for 30 mins at 210ºC and subsequent exposed to the EXCO solution for 4 h. The ST and LS planes after 30 mins of aging seem devoid of corrosion (Fig. 4.4). The pits have a depth of 100,44 μm (Fig. 4.4 c) in the ST plane and 88,45μm (Fig 4.15**Error! Reference source not found.** e) in the LS plane. So it seems that there is some corrosion activity after 30 mins aging and 4 h exposure time.

| ST plane | LS plane |
|---|---|
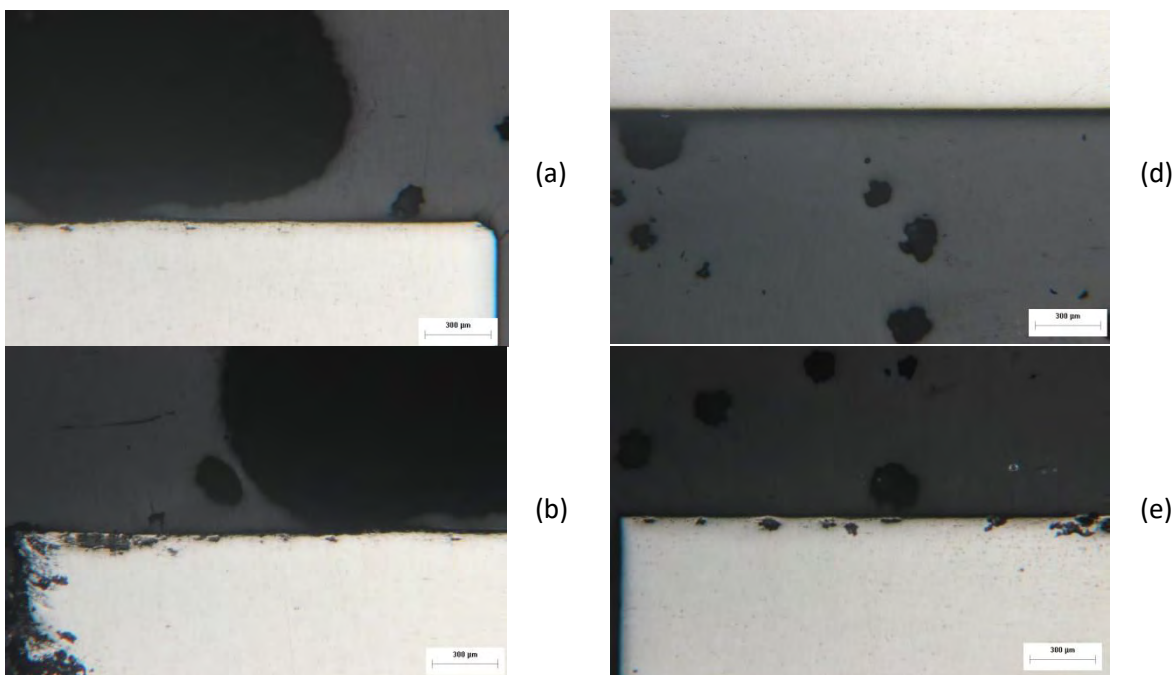
Fig. 4.15: Exfoliation corrosion for alloy 2024-T351 after aging for 30 mins at T=210ºC. Images (a) to (c) depict exfoliation in the ST plane and images (d) to (f) depict exfoliation in the LT plane. Magnification is x50. Maximum depth of attack was measured 100,44 μm at fig (c).

### Aging time 1 hour

After 1 hour aging, pitting density seems to increase and pits grow deeper. The maximum pit depth was measured μm. A new feature is the grouping of pits, i. e pits that grow close to each other coalesce and form a larger corrosion area. Specifically images (a) to (c) depict exfoliation corrosion in the ST plane. Magnification is x50 and pits have maximum depth of 102,29 μm (Fig 4.16 b). Images (d) to (f) depict exfoliation in the LS plane. Magnification is x50 and the maximum depth of attack was measured 96,81 μm at (Fig 4.16 d)

**ST plane**    **LS plane**

(c)

(f)

Fig.4.16: Exfoliation corrosion for alloy 2024-T351 after aging for 1 hour at T=210°C. Images (a) to (f) depict exfoliation in the ST plane and in the LT plane respectively. Magnification is x50. Maximum depth of attack was measured 298,8 μm at fig (b) as illustrated in Table 3 .

*Aging time 2 hours*

After 2 hours aging, pitting density has not increased significantly and the pits do not grow deeper. Specifically images (a) to (f) depict exfoliation in the ST and LS plane respectively. Magnification is x50 and the maximum pit depth varies from 105,20 μm to 120,91 μm for the ST plane and LS plane respectively.

**ST plane**                    **LS plane**



(a)

(d)

(b)

(e)

(c)

(f)

Fig.4.17: Exfoliation corrosion for alloy 2024-T351 after aging for 2 h at T=210°C. Images (a) to (f) depict exfoliation in the ST plane and LT plane. Magnification is x50. Maximum depth of attack was measured 121,90 μm at fig (e) as illustrated in Table 3 .

*Aging time 4 hours*

After 4 hours aging, it is observed similar corrosion activity as for the previous aging times. Images (a) to (f) depict corrosion depth of attack in the ST and LS plane respectively. Magnification is x50 and maximum depth of attack was measured 196,97 μm (Fig 4.18 d).
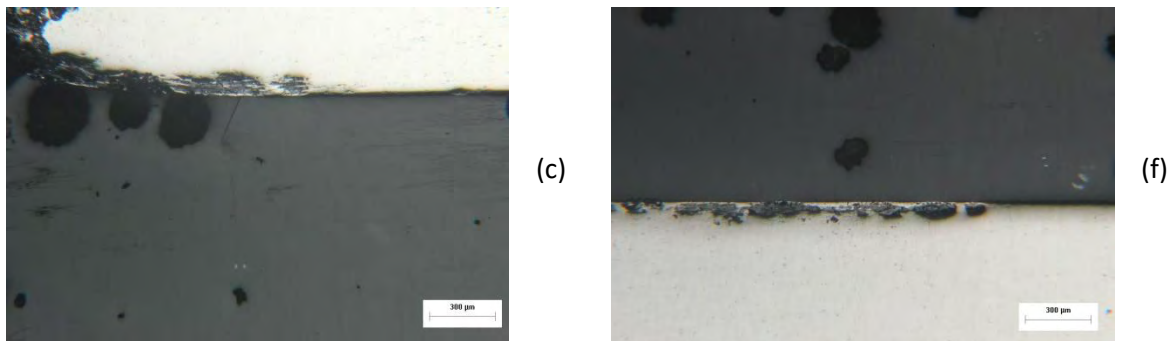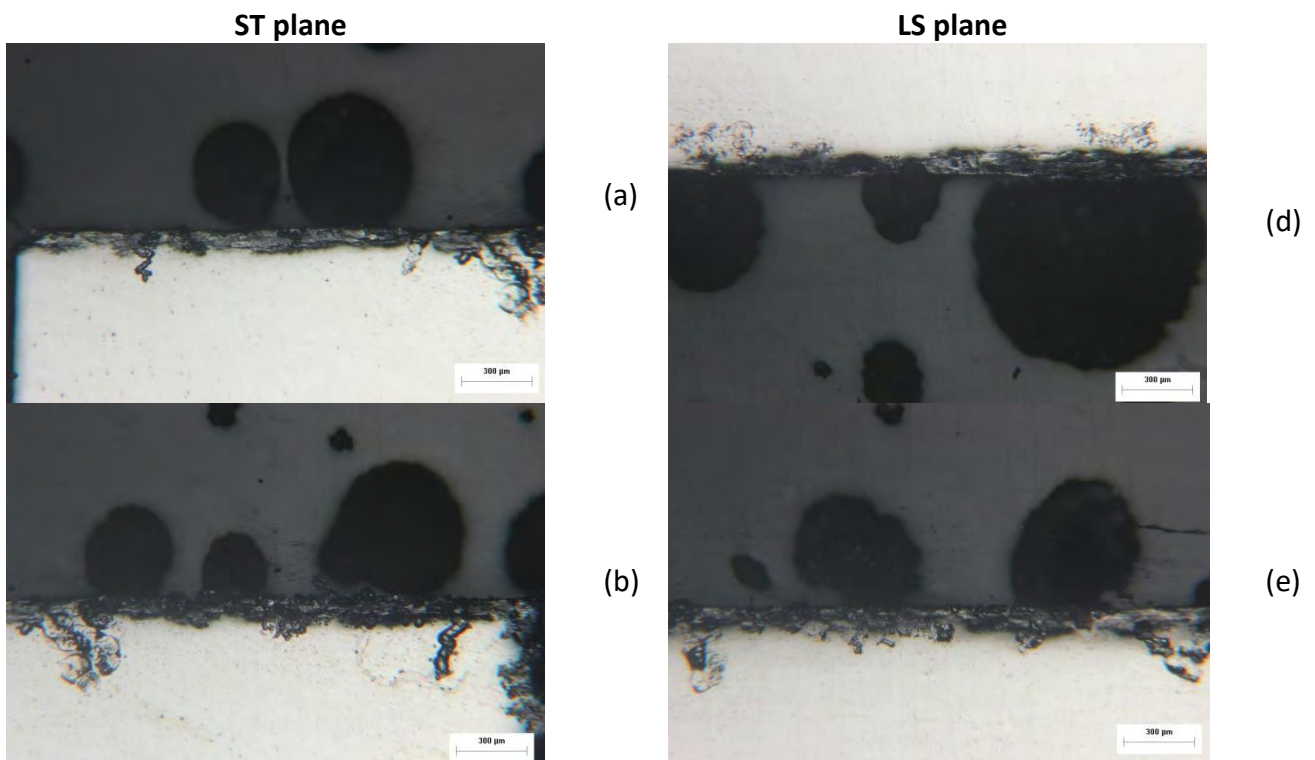
| **ST plane** | **LS plane** |
|---|---|



(a)

(d)

(b)

(e)

(c)

(f)

Fig. 4.18: Exfoliation corrosion for alloy 2024-T351 after aging for 4 h at T=210°C. Images (a) to (f) depict exfoliation in the ST and LT plane. Magnification is x50. Maximum depth of attack was measured 256,97 μm at fig (d) as illustrated in Table 3 .


### *Aging time 6 hours*

After 6 hours aging, corrosion pits cover the entire surface. Pits are larger and the clustering of pits is enhanced (Fig 4.19). Exfoliation corrosion becomes quite severe (Fig 4.19 b). Specifically images (a) to (f) depict exfoliation in the ST and LT plane. Magnification is x50. Maximum depth of attack was measured 200,79 μm, at fig(c)  as illustrated in Table 3 .
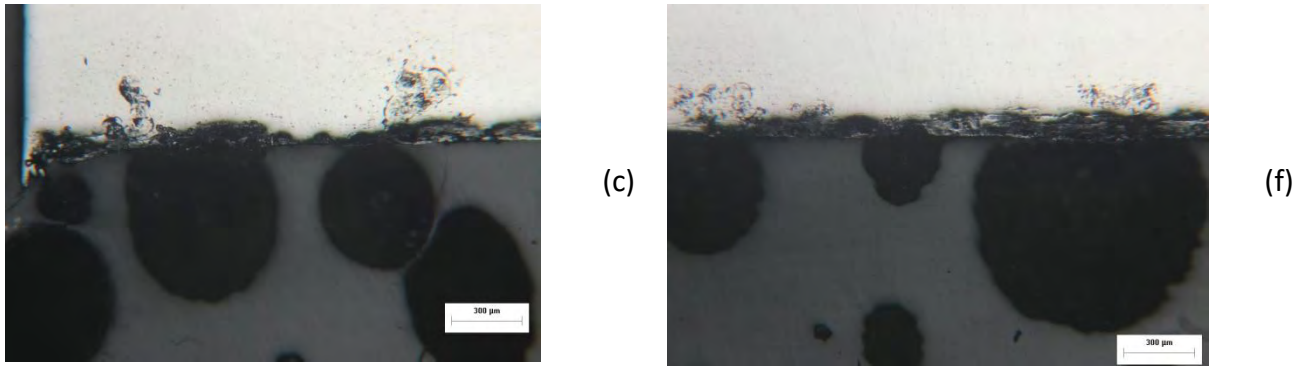

**ST plane**  **LS plane**



(a)

(d)

(b)

(e)

(c)



(f)

Fig. 4.19: Exfoliation corrosion for alloy 2024-T351 after aging for 6 h at T=210°C. Images (a) to (f) depict exfoliation in the ST and LT plane. Magnification is x50. Maximum depth of attack was measured 200,79 μm, at fig(c) as illustrated in Table 3 .

*Aging time 9 hours*

After 9 hours aging, images (a) to (f) depict exfoliation in the ST and LT plane. Magnification is x50. Maximum depth of attack was measured 212,75 μm, as illustrated in Table 3 .

**ST plane**

**LS plane**



(a)



(d)

(b)

(e)

(c)



(f)
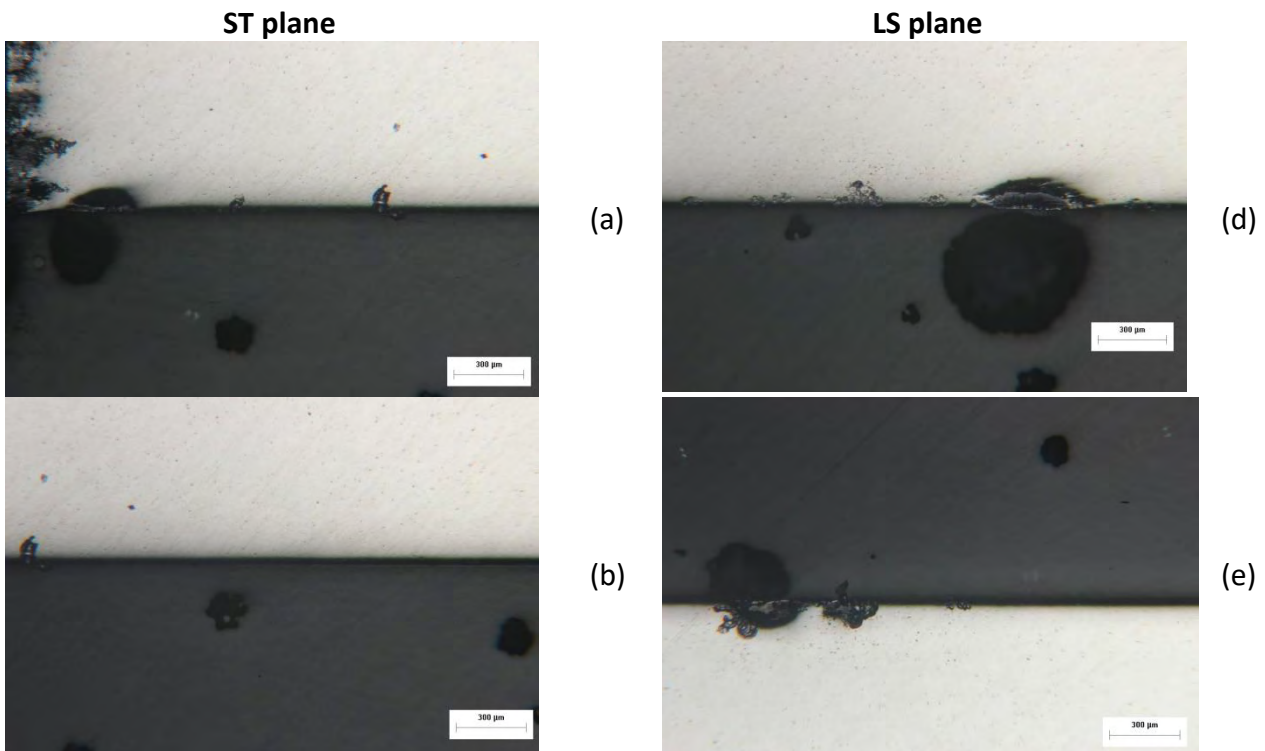
Fig4.20: Exfoliation corrosion for alloy 2024-T351 after aging for 9 h at T=210$^{\circ}$C. Images (a) to (f) depict exfoliation in the ST and LT plane. Magnification is x50. Maximum depth of attack was measured 212,75 μm, as illustrated in Table 3 .

### *Aging time 15 hours*

After 15 hours aging, images (a) to (f) depict exfoliation in the ST and LT plane. Magnification is x50. Maximum depth of attack was measured 219,92 μm at fig (b) as illustrated in Table 3 .

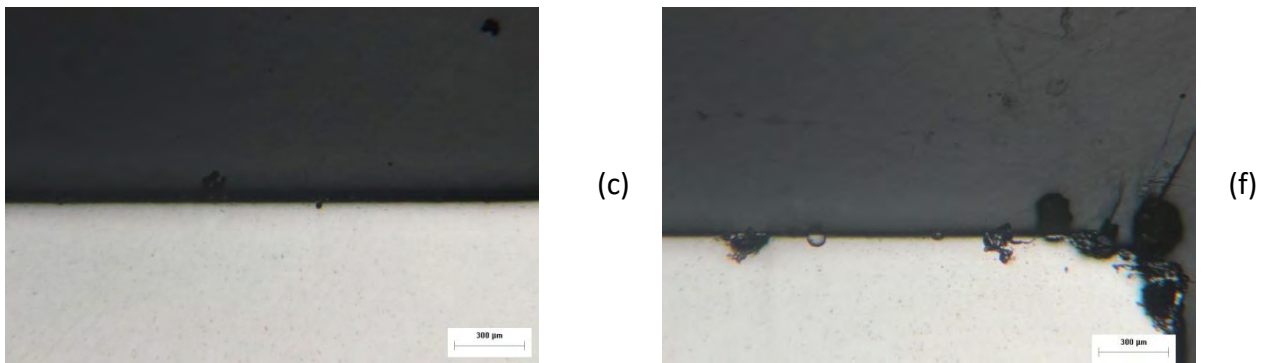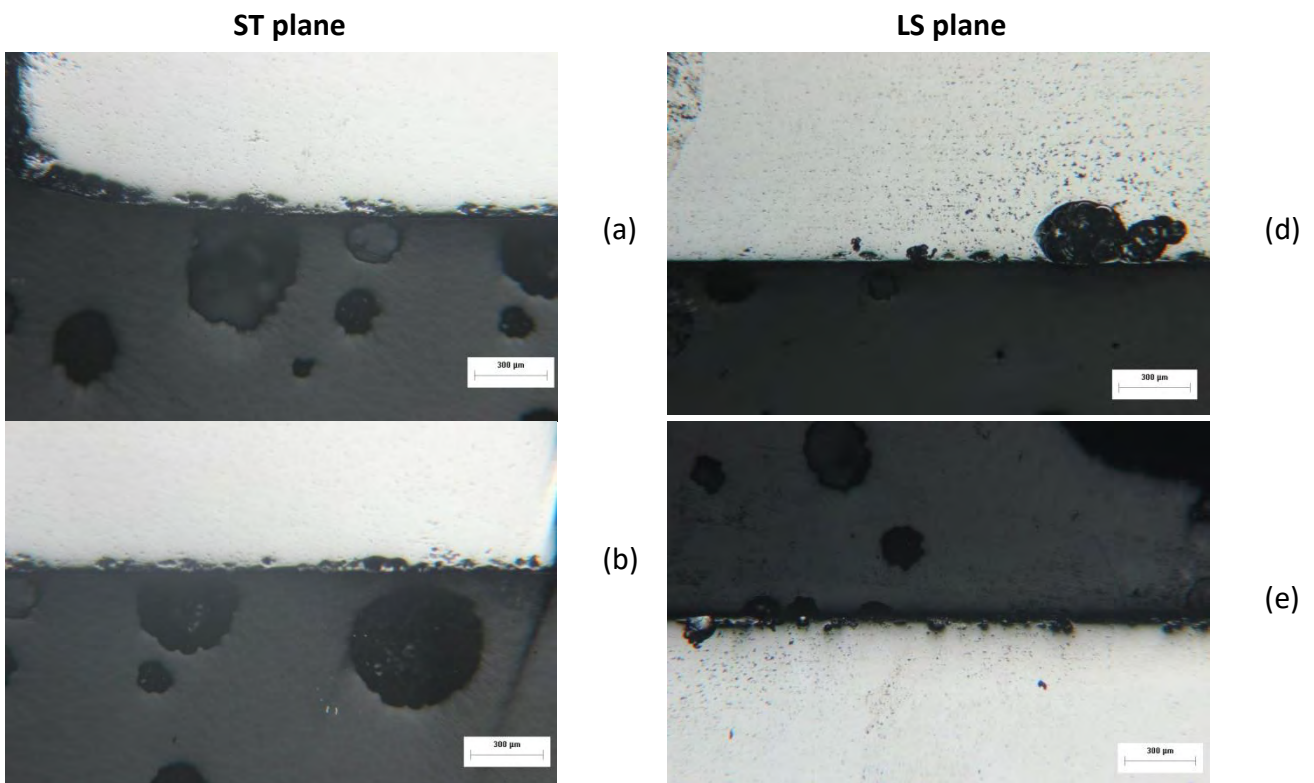**ST plane**

**LS plane**



(a)



(d)



(b)



(e)

(c)



(f)
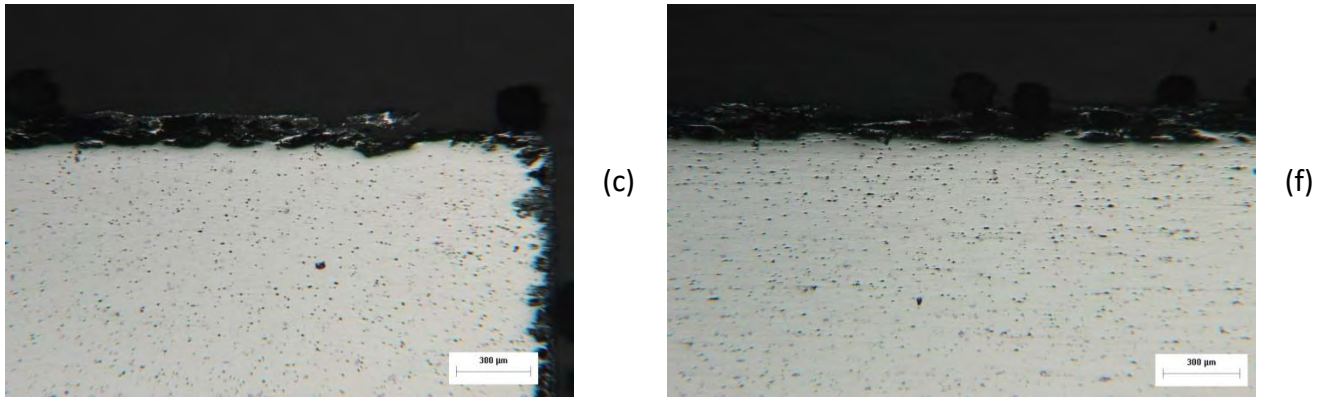
Fig. 4.21: Exfoliation corrosion for alloy 2024-T351 after aging for 15 h at T=210°C. Images (a) to (f) depict exfoliation in the ST and LT plane. Magnification is x50. Maximum depth of attack was measured 219,92 μm at fig (b) as illustrated in Table 3 .

*Aging time 24 hours*

After 24 hours aging, images (a) to (f) depict exfoliation in the ST and LT plane. Magnification is x50. Maximum depth of attack was measured 114,74 μm at fig.(c) or 156,57 μm at fig.(f) as illustrated in Table 3 .

**ST plane**

**LS plane**



(a)



(d)



(b)



(e)

(c)



(f)
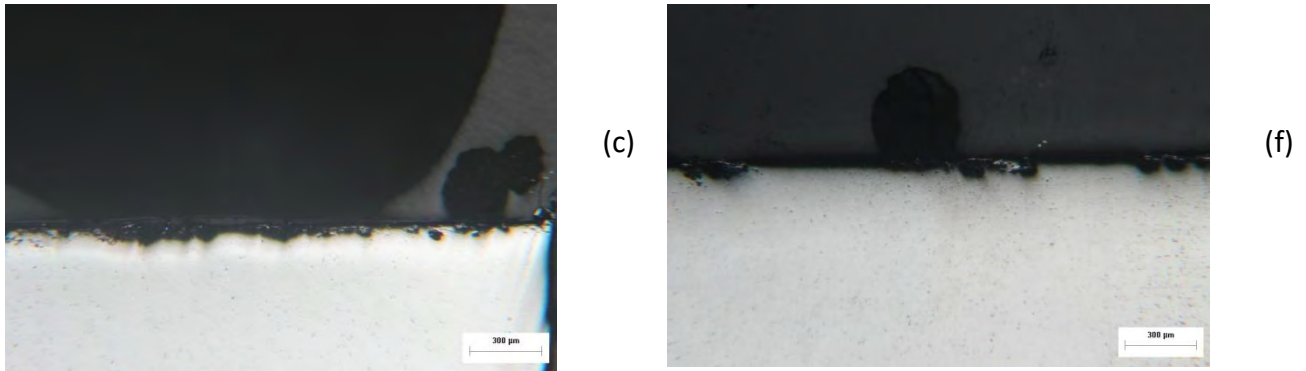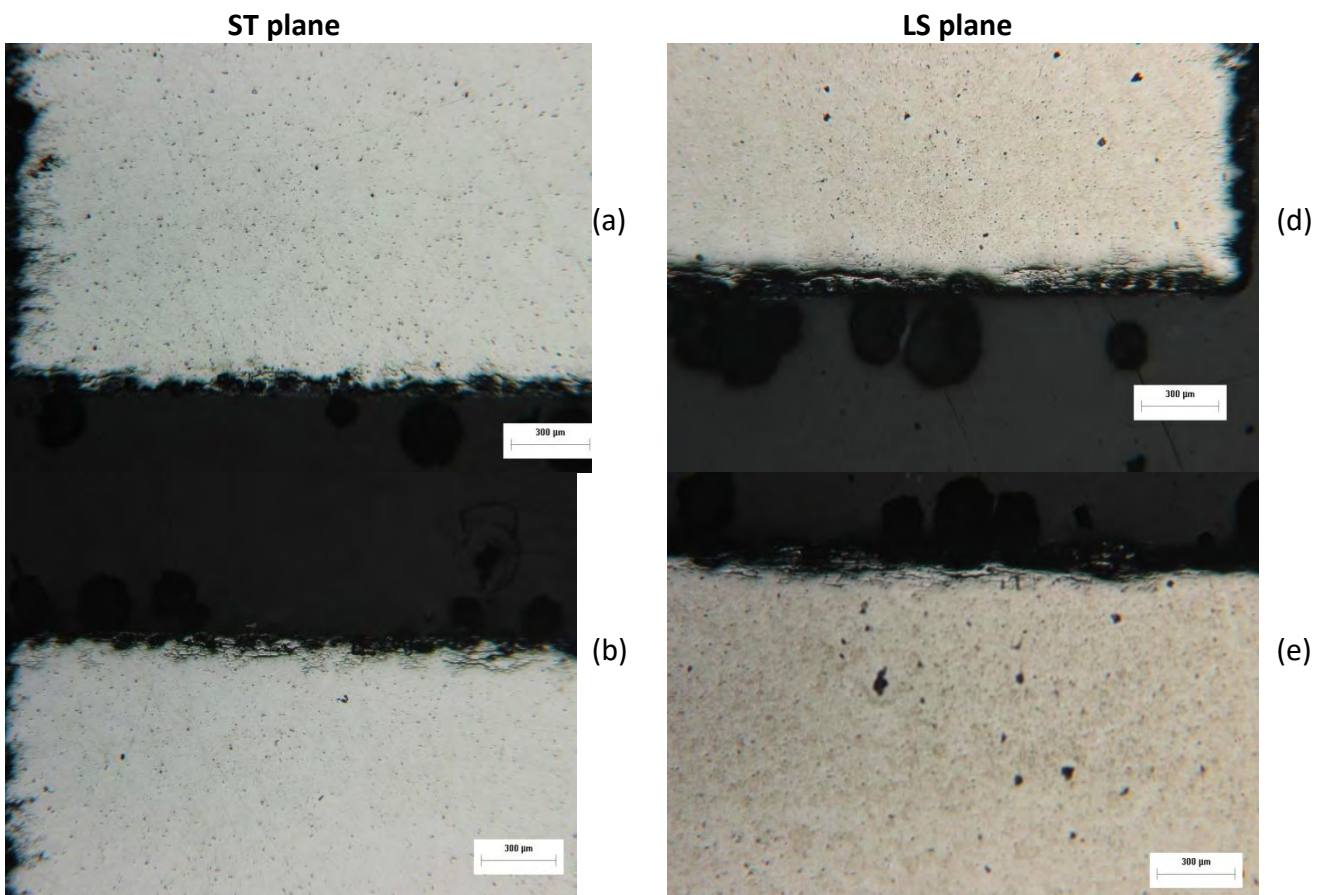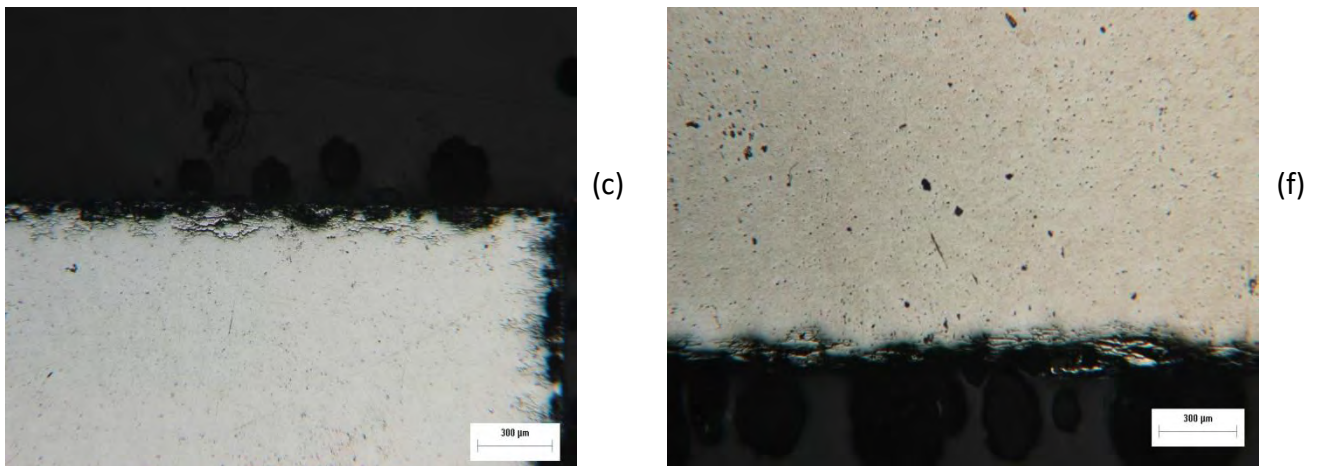
Fig.4.22: Exfoliation corrosion for alloy 2024-T351 after aging for 24 h at T=210°C. Images (a) to (f) depict exfoliation in the ST and LT plane. Magnification is x50. Maximum depth of attack was measured 114,74 μm at fig.(c) or 156,57 μm at fig.(f) as illustrated in Table 3 .

*Aging time 36 hours*

After 36 hours aging, images (a) to (f) depict exfoliation in the ST plane. Magnification is x50. Maximum depth of attack was measured 216,33 μm at fig (e) as illustrated in Table 3 .

**ST plane**

**LS plane**



(a)



(d)



(b)



(e)
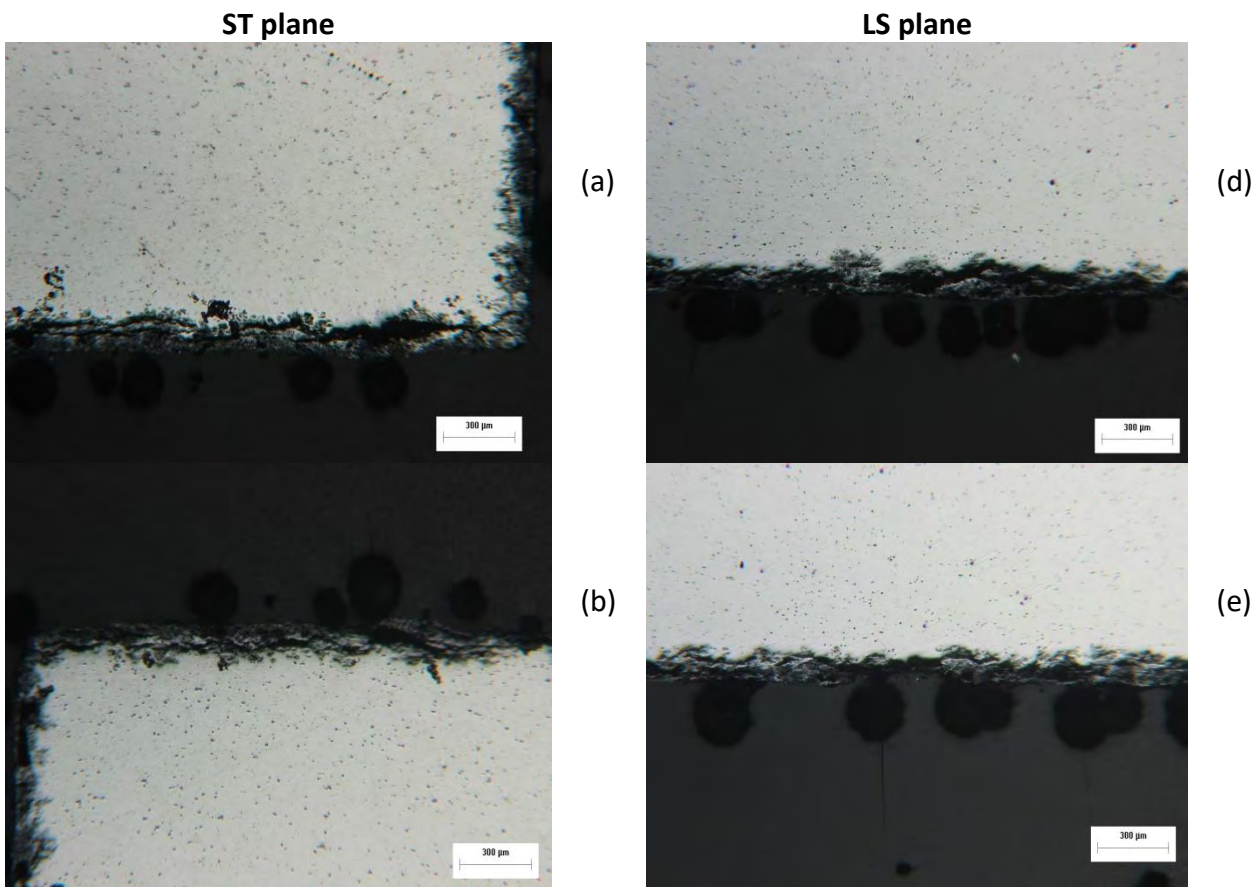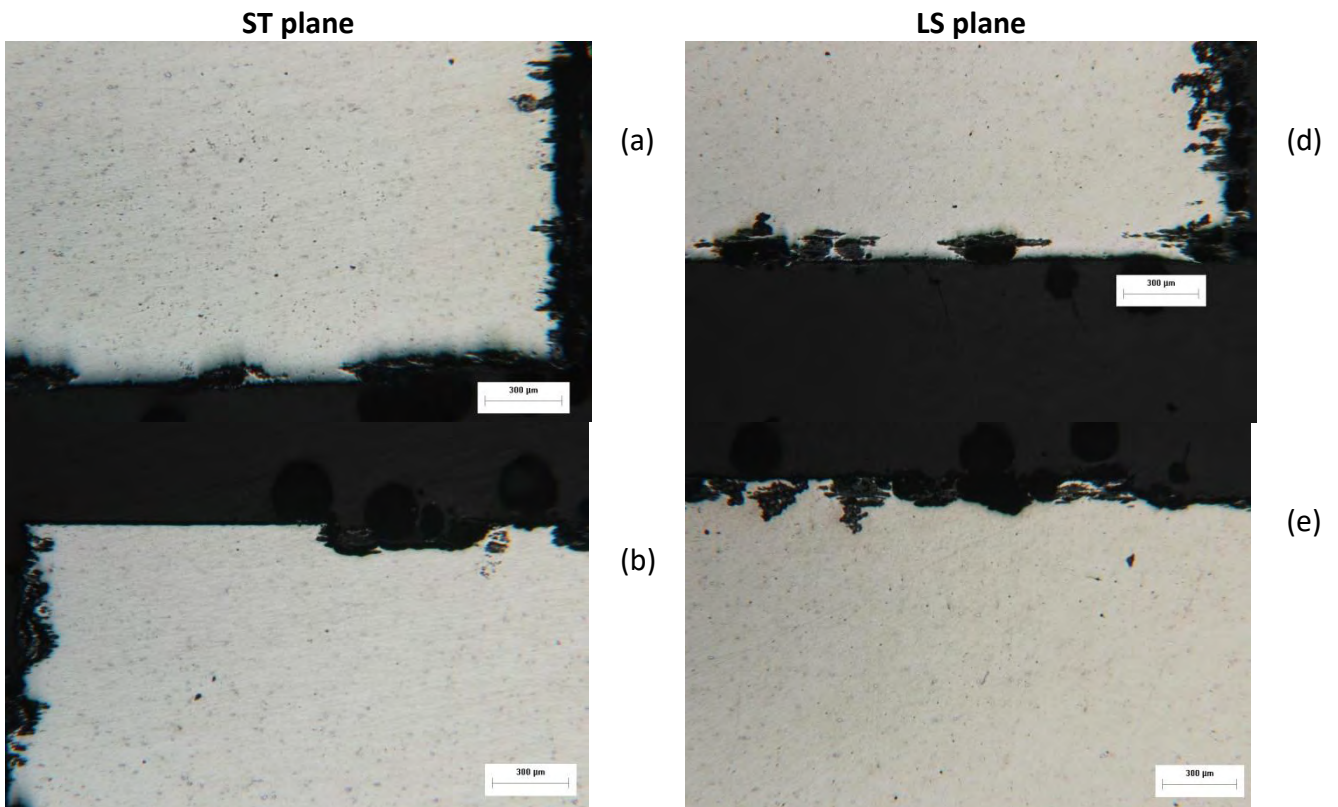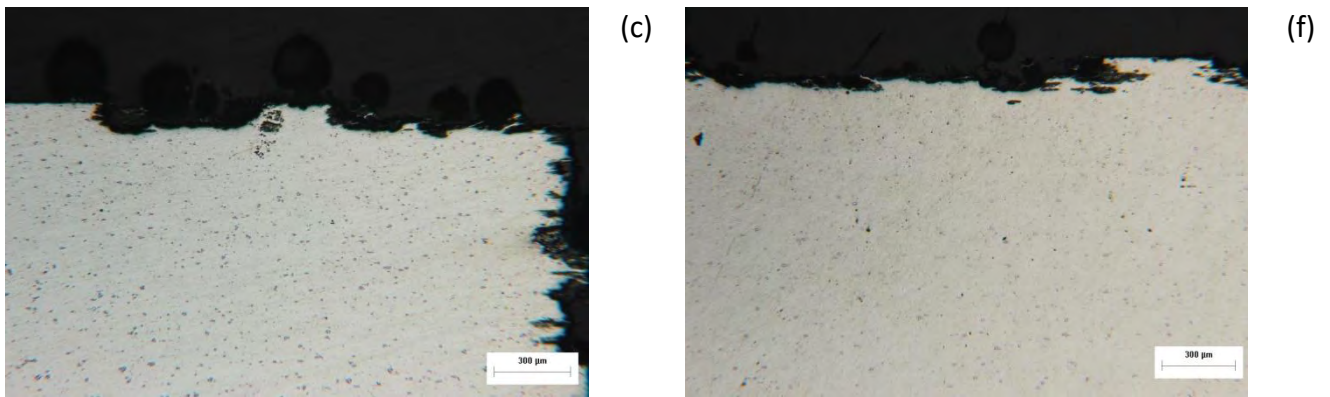
Fig4.23: Exfoliation corrosion for alloy 2024-T351 after aging for 36 h at T=210°C. Images (a) to (f) depict exfoliation in the ST plane. Magnification is x50. Maximum depth of attack was measured 216,33 µm at fig (e) as illustrated in Table 3 .

### Aging time 48 hours

After 48 hours aging, images (a) to (f) depict exfoliation in the ST and LT plane. Magnification is x50. Maximum depth of attack was measured 194,82 µm at fig (a) as illustrated in Table 3 .
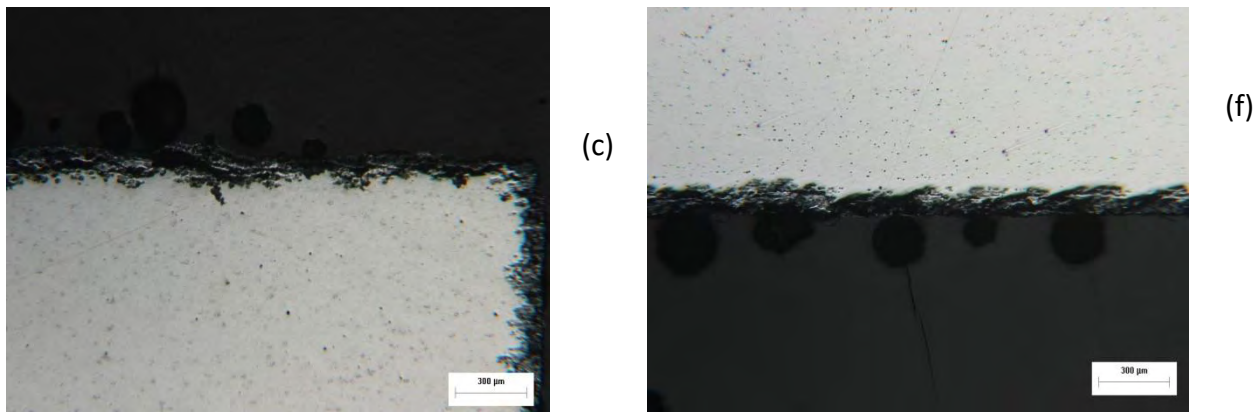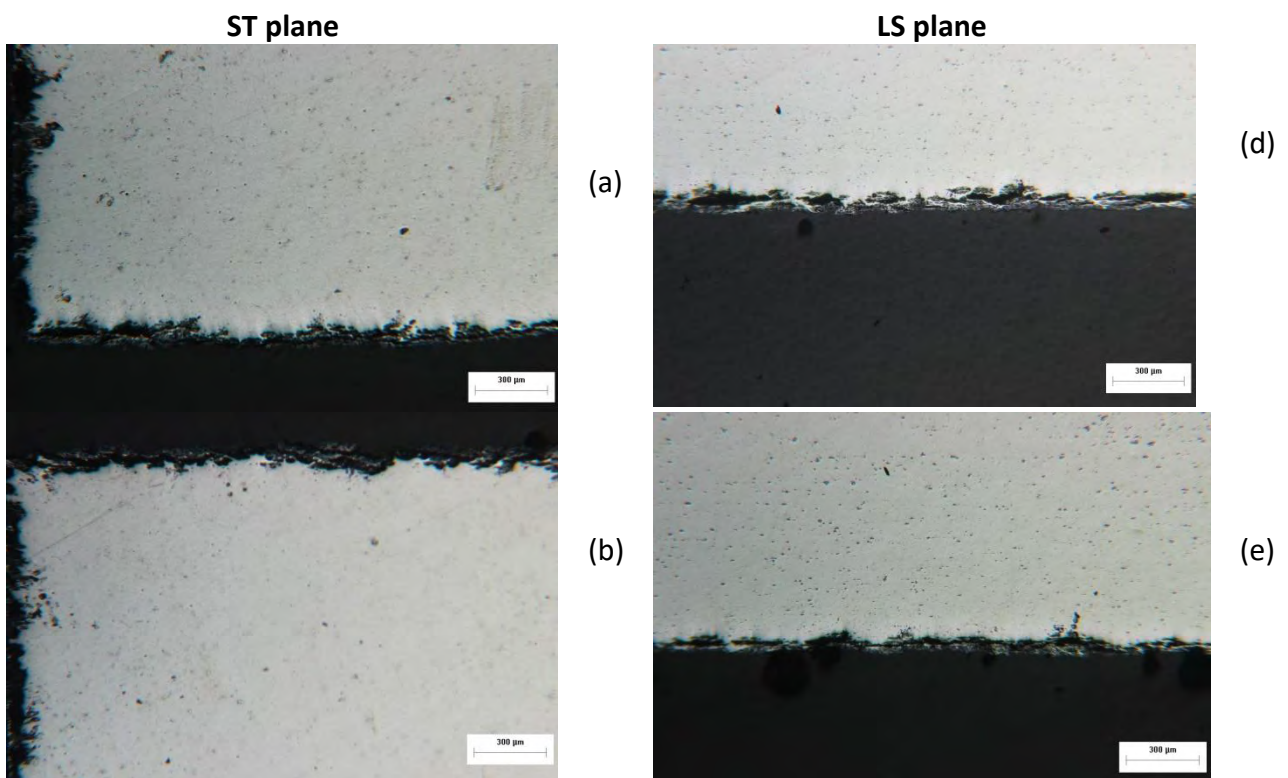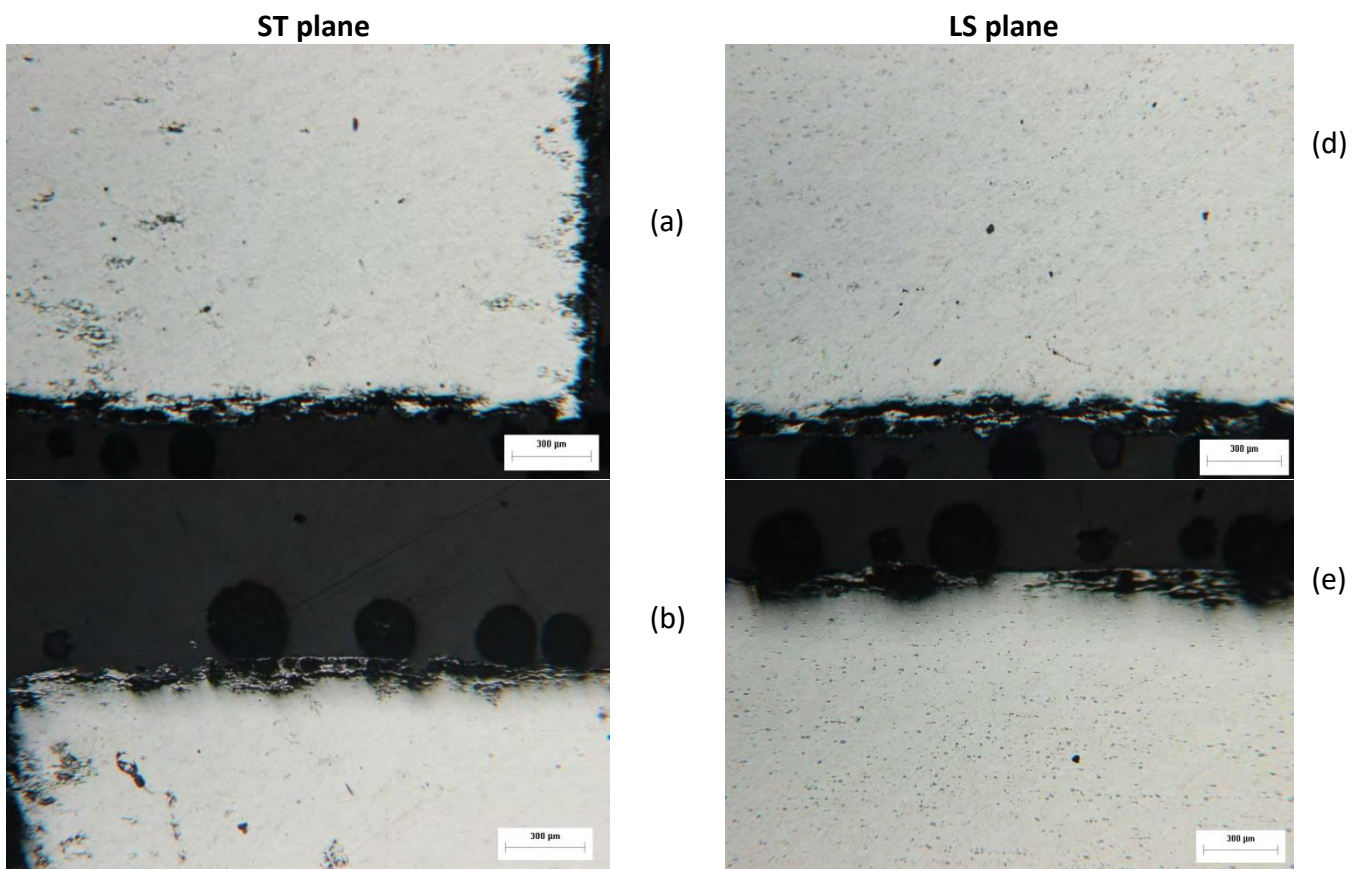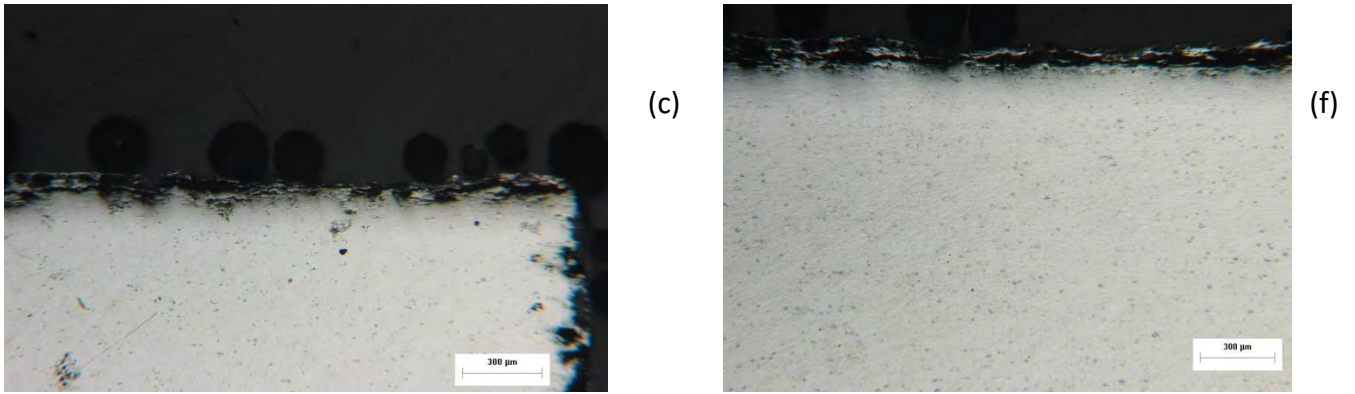
Fig.4.24: Exfoliation corrosion for alloy 2024-T351 after aging for 48 h at T=210°C. Images (a) to (f) depict exfoliation in the ST and LT plane. Magnification is x50. Maximum depth of attack was measured 194,82 μm at fig (a) as illustrated in Table 3 .

*Aging time 54 hours*

After 54 hours aging, images (a) to (f) depict exfoliation in the ST and LT plane. Magnification is x50. Maximum depth of attack was measured 211,55 μm  at fig (e) as illustrated in Table 3 .

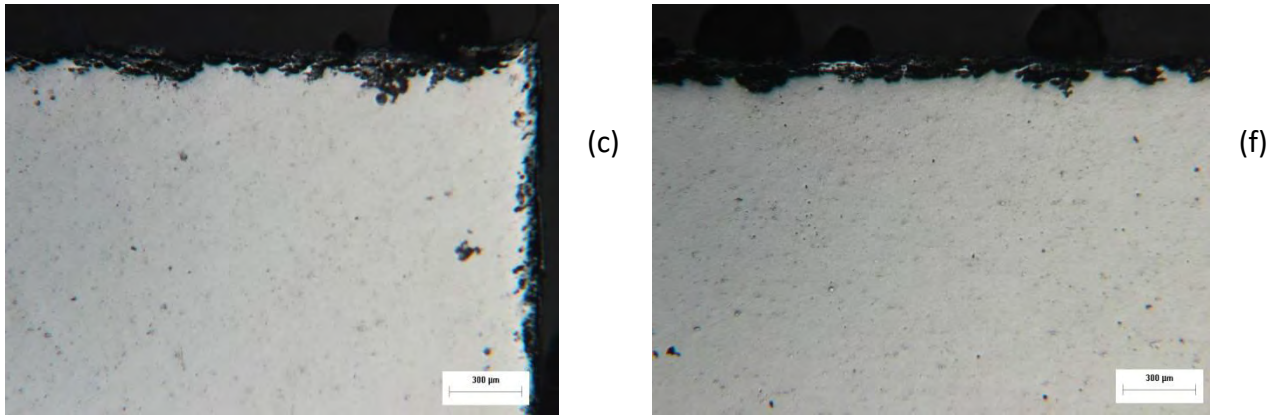**ST plane**               **LS plane**

(c)



(f)
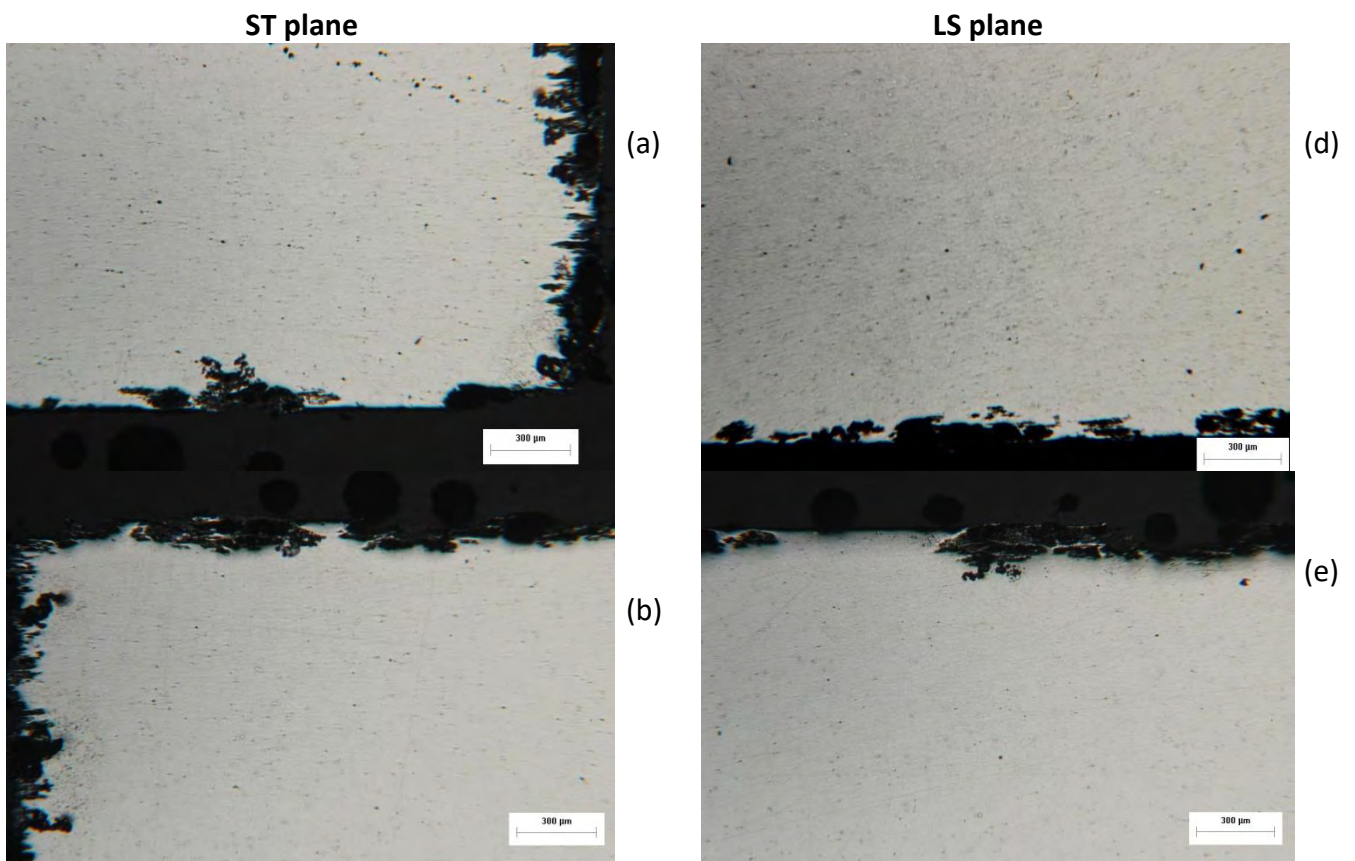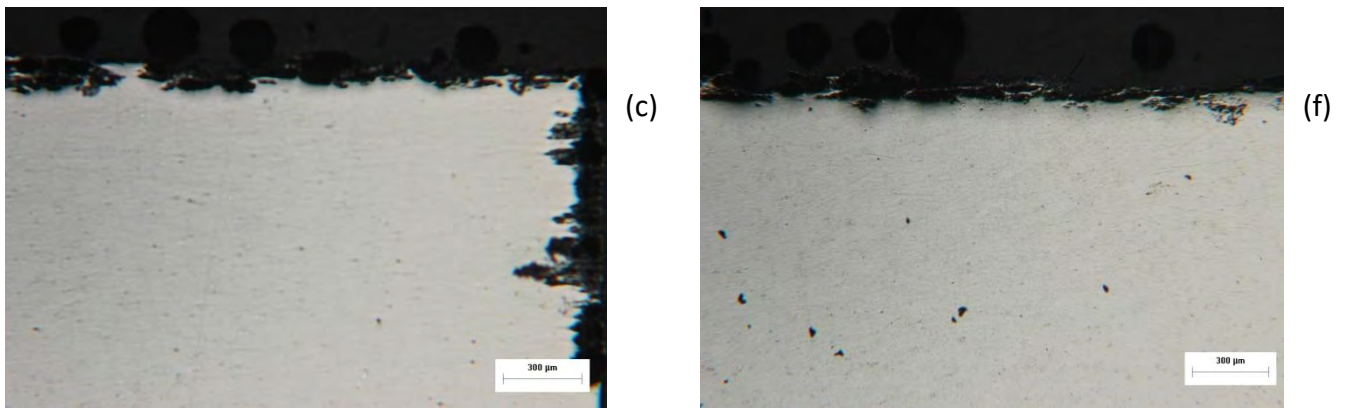
Fig.4.25: Exfoliation corrosion for alloy 2024-T351 after aging for 54 h at T=210°C. Images (a) to (f) depict exfoliation in the ST and LT plane. Magnification is x50. Maximum depth of attack was measured 211,55 μm at fig (e) as illustrated in Table 3 .

*Aging time 63 hours*

After 63 hours aging, Images (a) to (f) depict exfoliation in the ST and LT plane. Magnification is x50. Maximum depth of attack was measured 160 μm at fig (a) as illustrated in Table 1 .

**ST plane**

**LS plane**
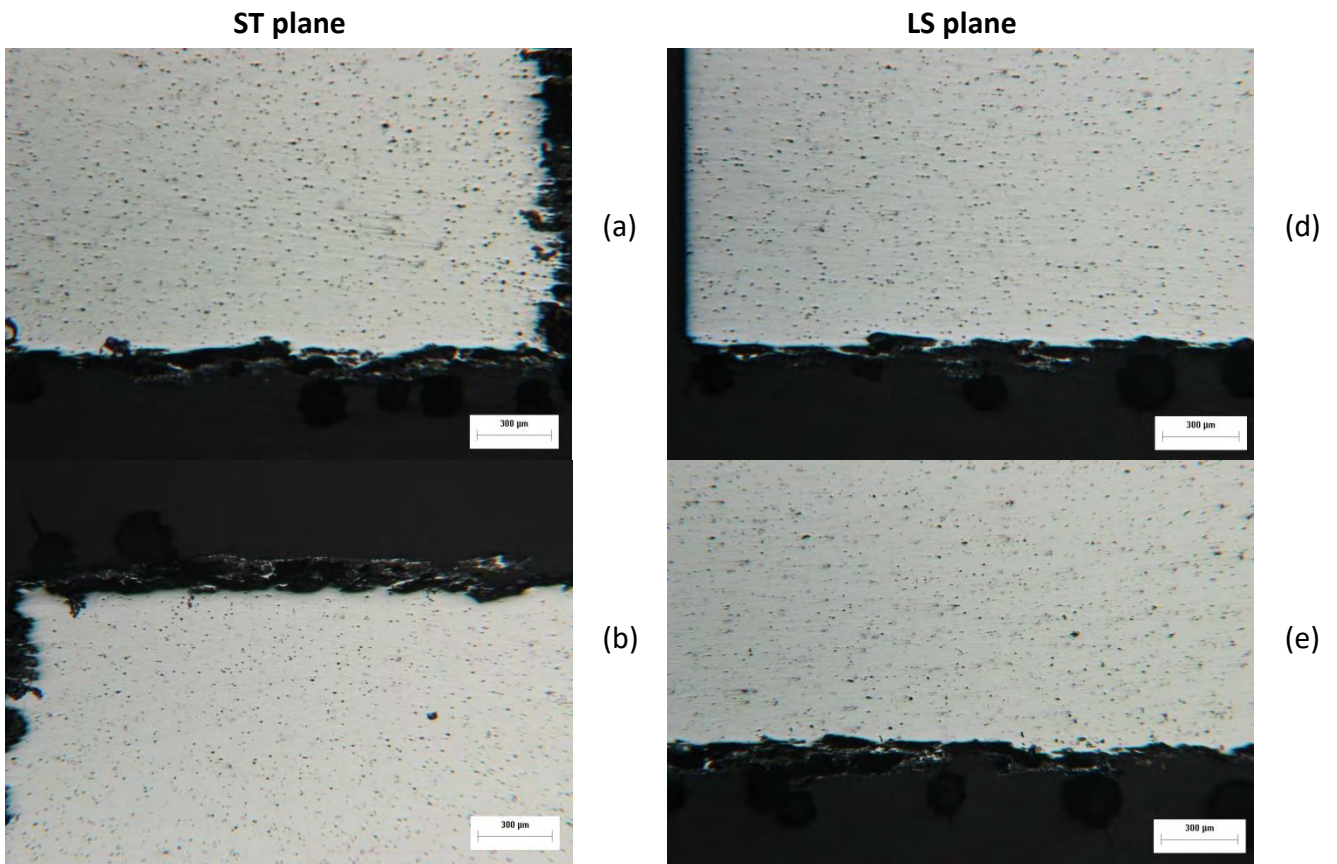


(a)



(d)



(b)



(e)
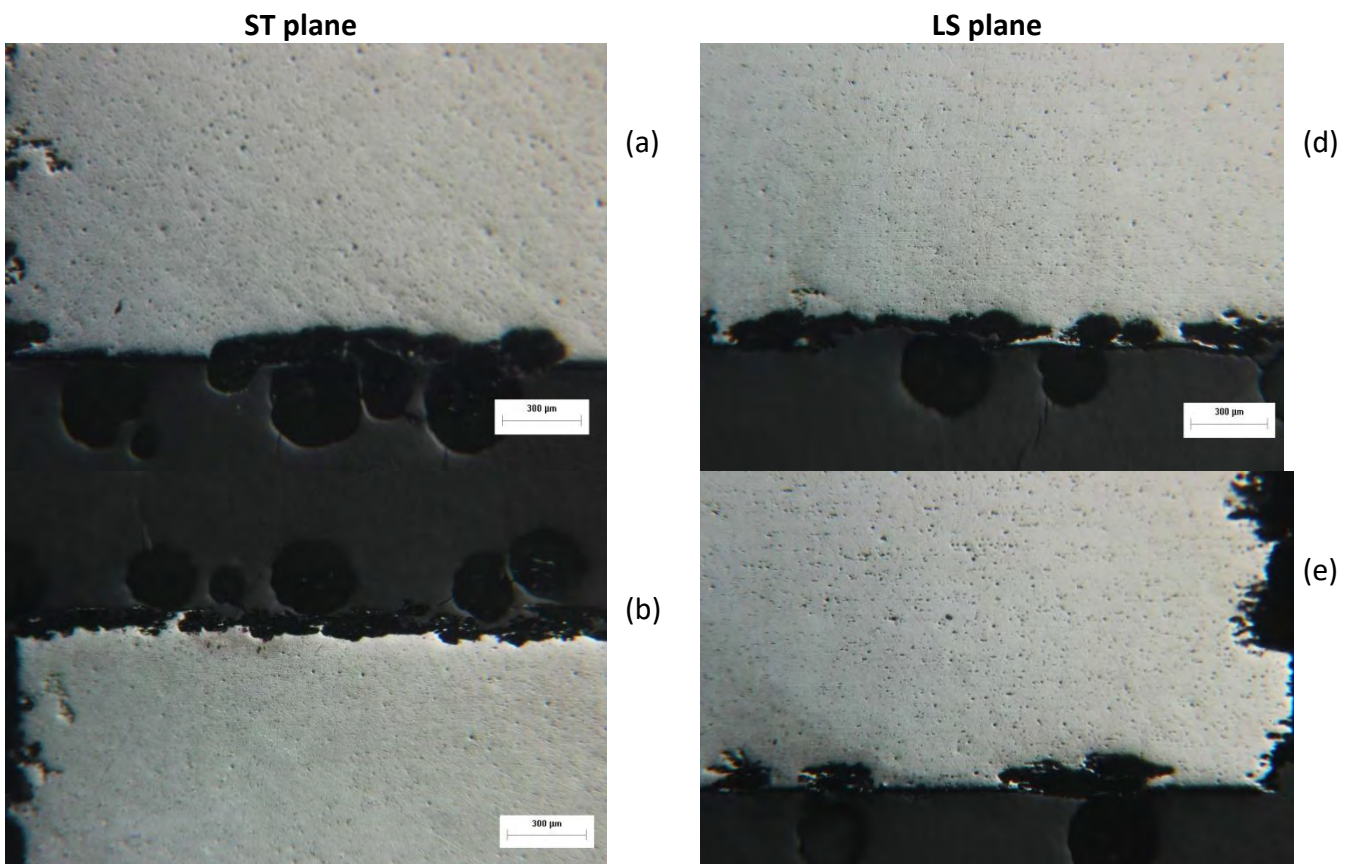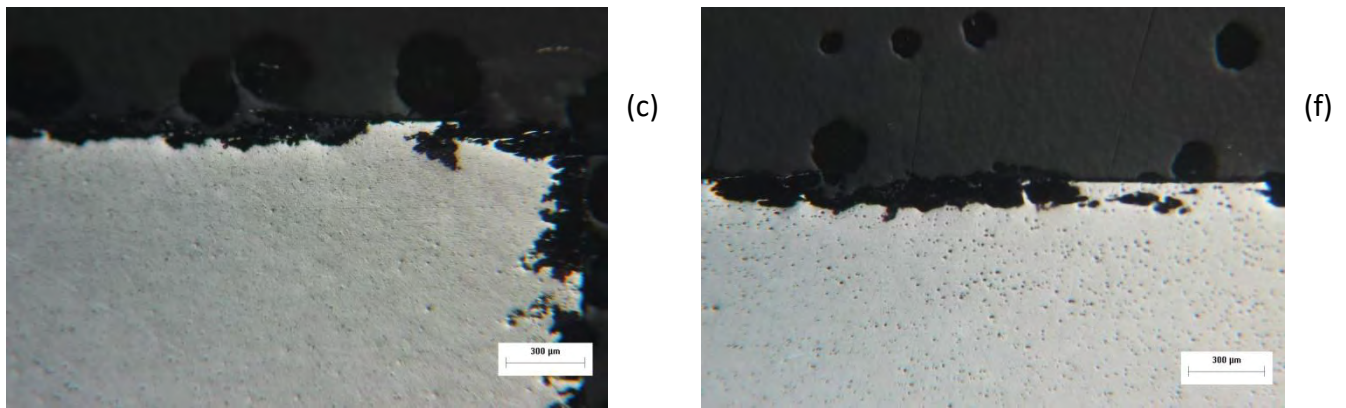
Fig.4.26: Exfoliation corrosion for alloy 2024-T351 after aging for 63 h at T=210°C. Images (a) to (f) depict exfoliation in the ST and LT plane. Magnification is x50. Maximum depth of attack was measured 160 μm at fig (a) as illustrated in Table 2. 3 .

In table 3 and figure 4.27 the maximum depth of attack versus aging time for the ST and LS planes is presented. It is observed that for 30min aging time and up to 4hours the maximum depth is near 100 μm. For 6 hours aging time to 64hours the maximum depth is around 200μm and is almost stable up to 63 hours. As is evident from figure 4.27 the depth of attack remains almost constant at 200 μm, with two maxima at 4 and 6 hours of aging.

Table 4. 1: Maximum depth of attack for the different times of aging and for the ST and LS side respectively, after 4 hours of EXCO exposure

| Time | ST plane | LS plane |
|------|----------|----------|
| 0.5 h | 100,44 | 88,44 |
| 1 h | 102,29 | 96,81 |
| 2 h | 105,20 | 121,91 |
| 4 h | 112,08 | 196,97 |
| 6h | 200,79 | 156,57 |
| 9 h | 212,75 | 178,09 |
| 15 h | 219,92 | 173,30 |
| 24 h | 114,74 | 157,57 |
| 36 h | 144,64 | 216,33 |
| 48 h | 194,82 | 167,32 |
| 54 h | 196,01 | 211,55 |
| 63 h | 147 | 160 |
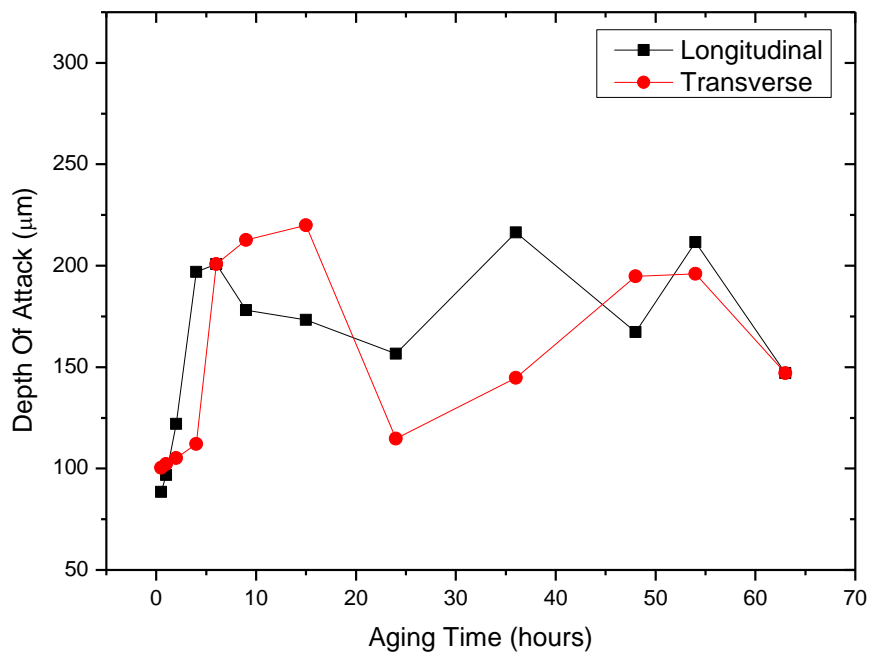
Fig.4.27: Maximun depth of attack for the different times of aging for the ST and LS plane after 4 hours of EXCO exposure.

The following figure 4.28 presents the material weight loss versus aging time. Two peaks are evident at 6 and 48 hours that correspond to the maximum depth of attack in figure 4.27
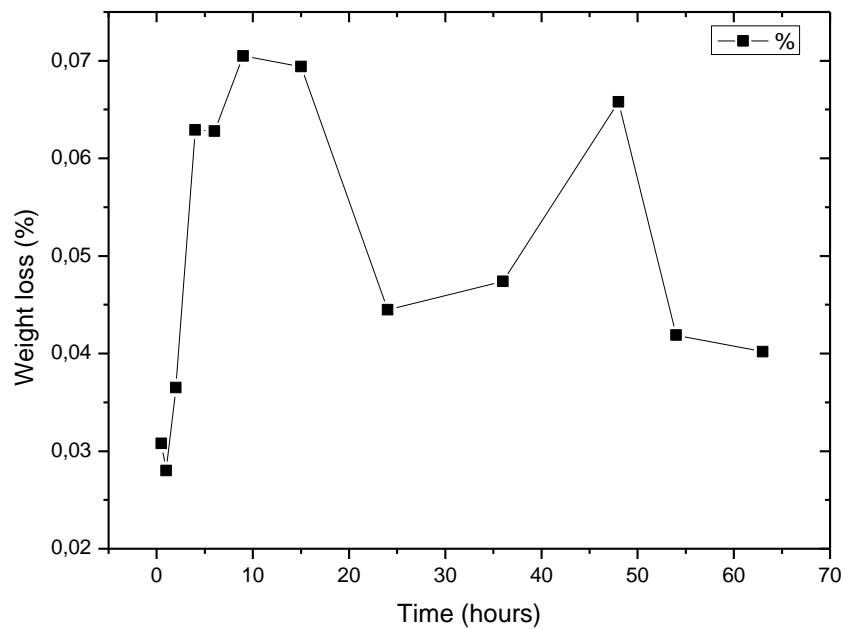


Fig. 4.28: Weight loss percentage of the specimens, that were introduced in the EXCO solution for 4 hours after aging in different conditions.

## 4.3 Microhardness measurements

Specimens of dimensions 5x10mm$^2$ were cut out of 2024 plate. The small size of the specimens was necessary for the uniform transport of heat into the sample during thermal treatment.

First, specimens were surface cleaned with alcohol according to ASTM G1 and then were heat treated. The specimens were artificially aged, after solid solution at 495°C for **30 mins**, at 170°C and 210°C respectively, in an electric oven with ± 4°C temperature control. The aging times for 170°C were 0.5 h, 1 h, 2 h, 4 h, 6 h, 9h, 12 h, 15 h, 24 h, 48 h, 63 h and 98 hours. Similarly the aging times for 210°C were 15 mins, 30 mins, 45 mins, 1 h, 2 h, 4 h, 6 h, 9 h, 15 h, 24 h, 36 h, 48 h, 54 h and 63 hours.

As is apparent from figure 4.29 the peak hardness of the material with aging at 170°C is between 9 and 12h while the peak hardness of the material with aging at 210°C is between 2 and 6 hours.
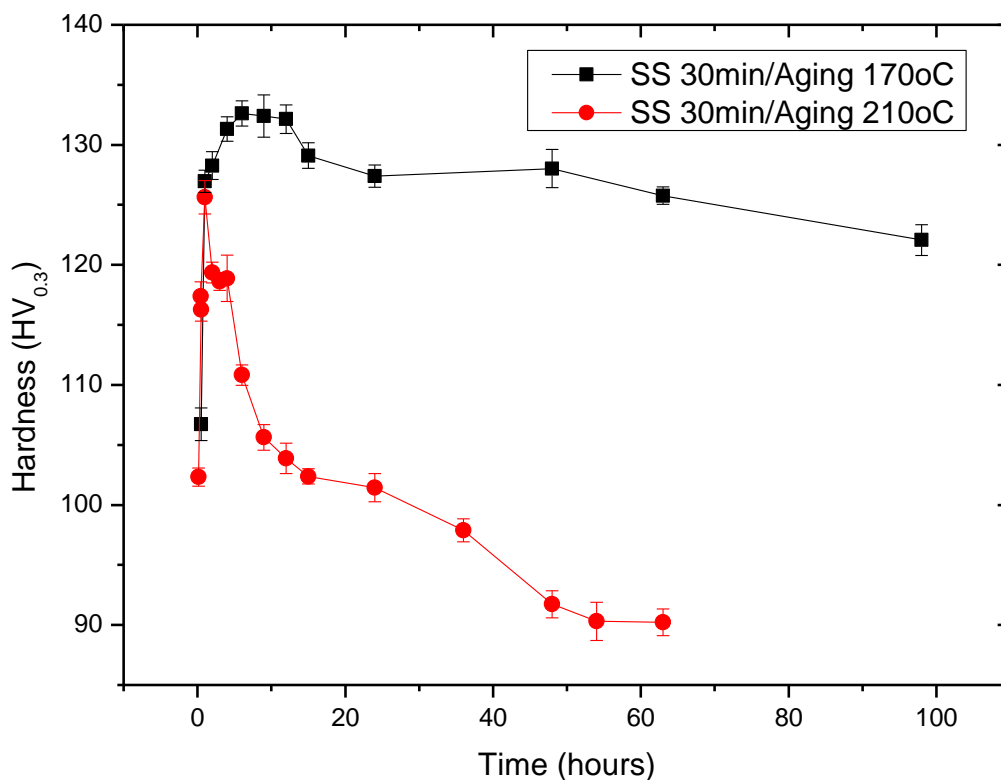


Fig. 4.29: Microhardness profile of 2024-T351 versus time of aging. The aging was performed at T=170°C for duration of 30 mins, 1 h, 2 h, 4 h,6 h, 9 h, 15 h , 24 h, 48 h, 63 h and 98 h respectively, as well as, at 210°C for duration of 15 min, 30 min, 45 mins, 1 h , 2 h, 3 h, 4 h, 6 h, 9 h, 15 h, 24 h, 36 h, 48 h, 54 h and 63 h respectively.

## 4.4 Hydrogen measurements

A main part of this thesis consists of the determination of hydrogen concentration and it's trapping states in the material after corrosion. The determination of these states was conducted by using a thermal desorption technique.

The results reported in the next section are presented as hydrogen mass flow rate (in μg/min) versus specimen temperature. If the heating rate is sufficiently low, each trapping site produces an independent peak. The temperature of the onset of peak growth is characteristic of the energy needed to release hydrogen from the respective trapping site. Thus, low temperature peaks are related to weakly bonded hydrogen and high temperature peaks to strongly bonded hydrogen. Calculation of the total hydrogen quantity in each trapping site is performed by integrating the area under the respective peak.

Experiments concerning hydrogen desorption from alloy 2024-T351 after exposure to the ECXO corrosive solution for the duration of 4 hours, at two different aging temperature exposures versus aging time were performed. The results are presented below. In accordance with previous work four distinct trapping states are observed.

Hydrogen is produced during the corrosion process and is being trapped in distinct energy states, which correspond to different microstructural traps. These traps are activated and liberate hydrogen at different temperatures. In alloy 2024, four traps T1 to T4 were identified. Trap T1 is considered to be a reversible trap, which liberates hydrogen continuously at low temperatures. Traps T2, T3 and T4 saturate with exposure time and are considered to be irreversible. In figure 4.30 the hydrogen spectra of specimen aged at 170°C and for times 30 mins, 1 h, 4 h, 9 h, 15 h, 24 h, 48 h, 63 h and 98 respectively are depicted.

Fig. 4.30: Spectrum of hydrogen evolved from the solution treated, quenched and aged specimens (SQA) after 4 hours exposure in EXCO solution. The specimens were artificially aged for 30 mins, 1 h, 4 h, 9 h, 15 h, 24 h, 48 h, 63 h and 98 respectively at 170°C.

Evaluating figure 4.30 in more detail it is observed that trapping state T3 exhibits a maxima for 15 hours of aging. For aging times larger than 24 hours there is a noted decline in hydrogen evolution for T3. Further investigation in the total quantity of hydrogen at each trapping state produced figures 4.31 to 4.34. Figure 4.31 depicts the total hydrogen content of corroded specimens in the T1 trapping state as a function of aging time. Trapping state T1 corresponds to hydrogen at interstitial sites. Figure 4.32 depicts the total hydrogen content of corroded specimens in the T2 trapping state as a function of aging time. Trapping state T2 is connected to the peak hardness of the materials [103]. From Fig. 4.29 it is evident that the peak hardness of the material is observed between 15 and 24h of aging.

Hydrogen is attracted to the strain fields associated with coherent and semi-coherent interfaces. As the particle size increases with aging time, the hardness increases due to coherency hardening, at the same time $H_2$ increases. After the peak, the interfaces loose coherency and the strain fields diminish. The hardness drops and follows Orowan-mechanism. At the same time, $H_2$ drops since $H_2$ is absorbed to the T4 state.

Fig.4 31: Total hydrogen content of corroded specimens in the T1 trapping state as a function of aging time (4 hours in the exfoliation solution).



Fig.4 32: Total hydrogen content of corroded specimens in the T2 trapping state as a function of aging time (4 hours in the exfoliation solution).

Figure 4.33 depicts the total hydrogen content of corroded specimens in the T3 trapping state as a function of aging time. It has been discussed in previous work that, T3 is associated with dislocation. Coherent / semicoherent interfaces are made up of dislocation arrays. As the particle size increases with aging time, the density of interfacial dislocation increases leading to increase in $H_2$ with aging

time. After the peak (15-24hours aging Fig. 4.29), the coherency is lost and the density of interfacial dislocation is reduced leading to a reduction of trapping hydrogen.



Fig.4 33: Total hydrogen content of corroded specimens in the T3 trapping state as a function of aging time (4 hours in the exfoliation solution).

Figure 4.34 depicts the total hydrogen content of corroded specimens in the T4 trapping state as a function of aging time. Trapping state T4 which is the strongest trap and its temperature range corresponds to the dissolution of the strengthening precipitate in alloy 2024, is associated with S particles.
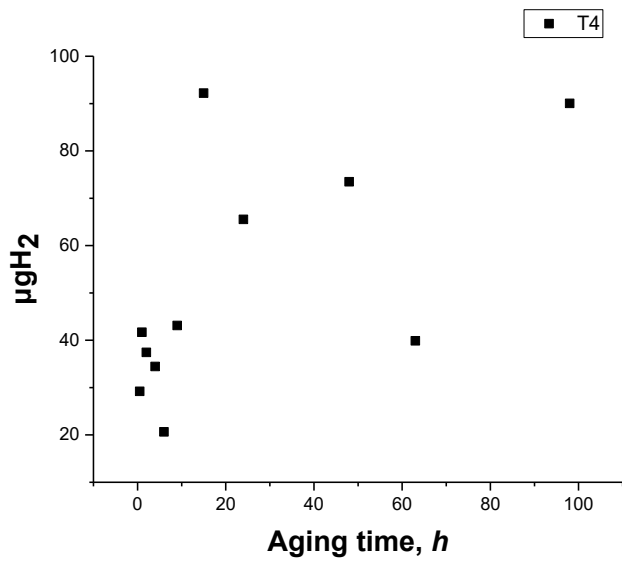


Fig.4 34: Total hydrogen content of corroded specimens in the T4 trapping state as a function of aging time (4 hours in the exfoliation solution).

A second heat treatment was applied to the material. Aging was performed at 210°C and for times 30 min, 1 h, 4 h, 9 h, 15 h, 24 h, 48 h, 63 h and 98 hours respectively. In figure 4.35 the hydrogen spectra of these specimens are depicted.
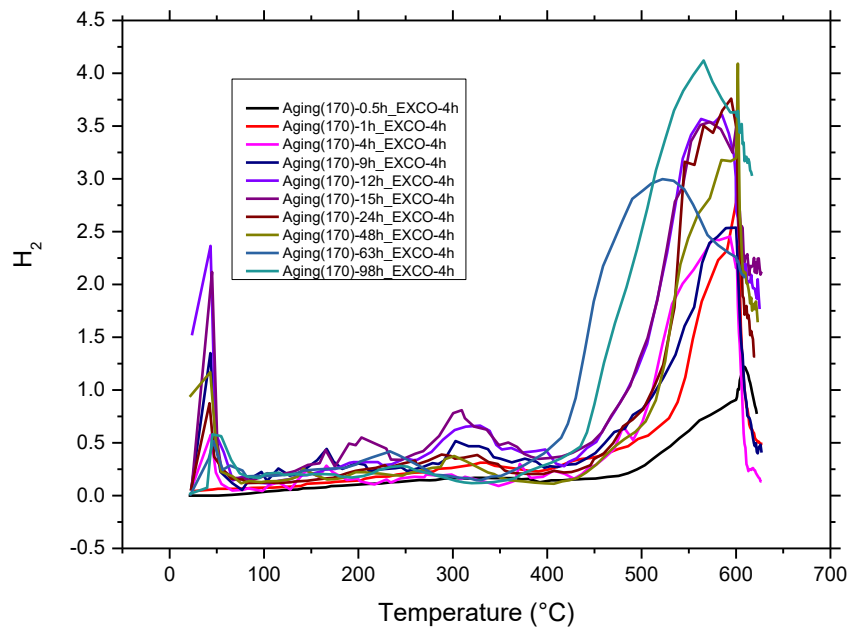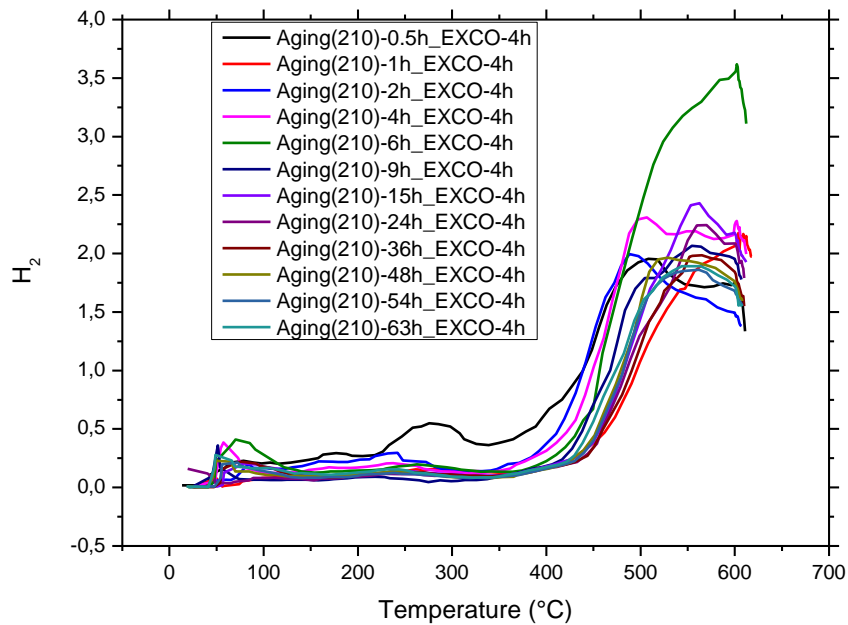


Fig. 4.35: Spectrum of hydrogen evolved from the solution treated, quenched and aged specimens (SQA) after 4 hours exposure in EXCO solution. The specimens were artificially aged for 30 mins, 1 h, 2 h, 4 h, 6 h, 9 h, 15 h, 24 h, 36 h, 48 h, 54 h and 63 h respectively at 210°C.

Further investigation in the total quantity of hydrogen at each trapping state produced figures 4.36 to 4.39. Figure 4.36 depicts the total hydrogen content of corroded specimens in the T1 trapping state as a function of aging time. Trapping state T1 corresponds to hydrogen at interstitial sites.

Figure 4.37 depicts the total hydrogen content of corroded specimens in the T1 trapping state as a function of aging time
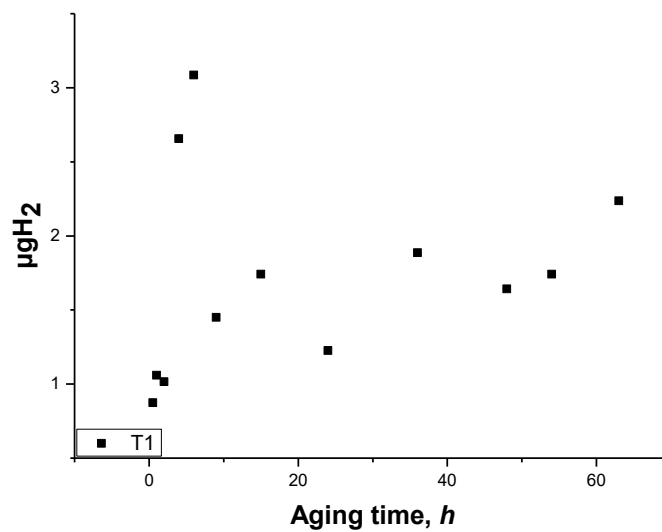
Fig.4 36: Total hydrogen content of corroded specimens in the T1 trapping state as a function of aging time (4 hours in the exfoliation solution, aging temperature 210°C).

Trapping state T2 is connected to the peak hardness of the materials. From Fig. 4.29 it is evident that the peak hardness of the material is observed between 4 and 9h of aging.
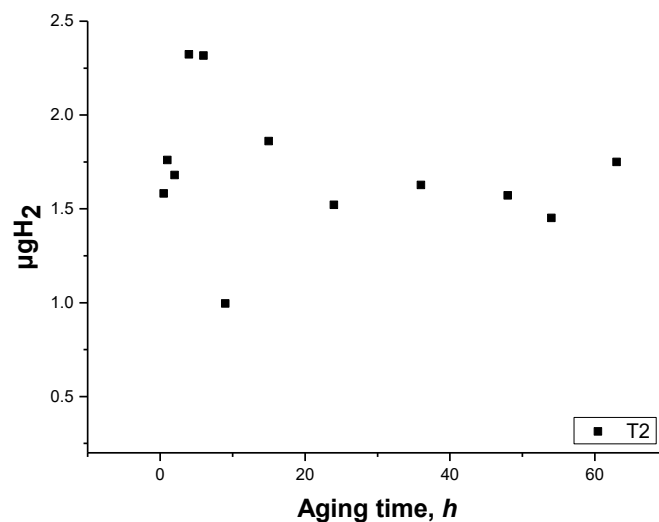


Fig.4 37: Total hydrogen content of corroded specimens in the T2 trapping state as a function of aging time (4 hours in the exfoliation solution, aging temperature 210°C).

Although as in the case of aging temperature 170°C a peak in hydrogen is connected with the peak aging condition (from microhardness measurements) the total quantity of hydrogen is less in the case of higher heating temperature 210°C. When specimens are aged at 170°C the maximum value is 7.5 $\mu gH_2$, while at 210°C it is 2.3 $\mu gH_2$. In previous work T2 was connected with the strain fields associated

with coherent and semi-coherent interfaces when aging is performed at higher temperatures fewer coherent and semi-coherent particles are formed and dissolve faster.

Figure 4.38 depicts the total hydrogen content of corroded specimens in the T3 trapping state as a function of aging time. It has been discussed in previous work that, T3 is associated with dislocation. Coherent / semicoherent interfaces are made up of dislocation arrays. As the particle size increases with aging time, the density of interfacial dislocation increases leading to increase in $H_2$ with aging time. After the peak (4-9hours aging Fig. 4.29), the coherency is lost and the density of interfacial dislocation is reduced leading to a reduction of trapping hydrogen.
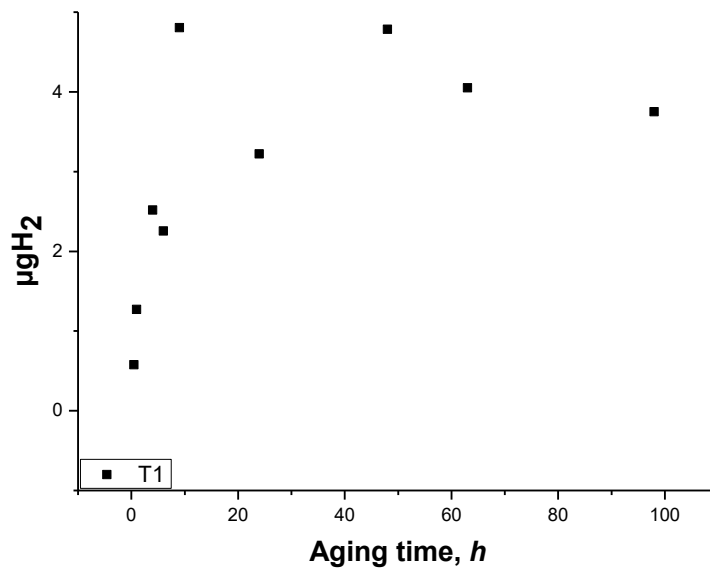


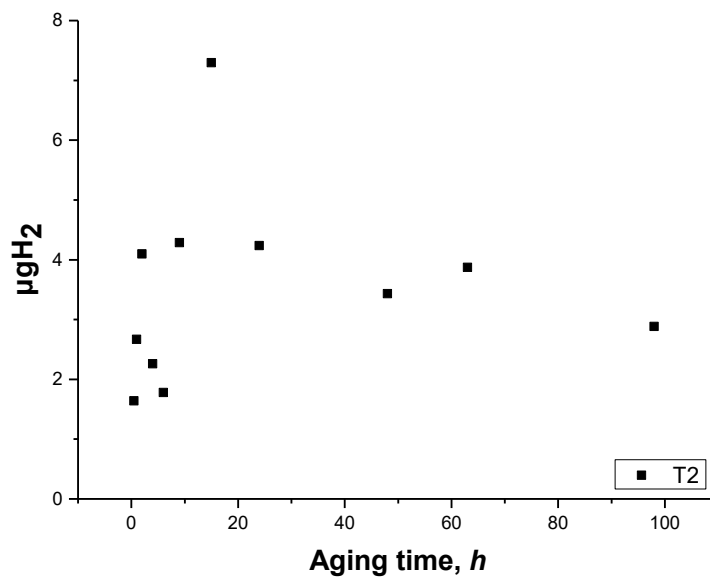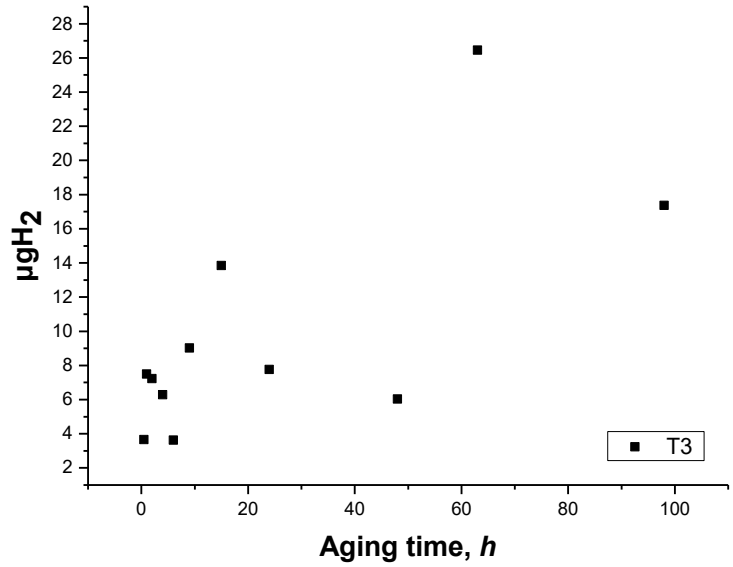Fig.4 38: Total hydrogen content of corroded specimens in the T3 trapping state as a function of aging time (4 hours in the exfoliation solution, aging temperature 210°C).

Figure 4.39 depicts the total hydrogen content of corroded specimens in the T4 trapping state as a function of aging time. Trapping state T4 which is the strongest trap and its temperature range corresponds to the dissolution of the strengthening precipitate in alloy 2024, is associated with S particles. During aging at 210°C the super saturation of solid solution is smaller than when aging at 170°C, thus the anticipated volume fraction of the S phase is also smaller. In consequence the total quantity of hydrogen absorbed in T4 is lower than in the case of 170°C, this is evident in figure 4.39 where the hydrogen content is much lower than in figure 4.34.
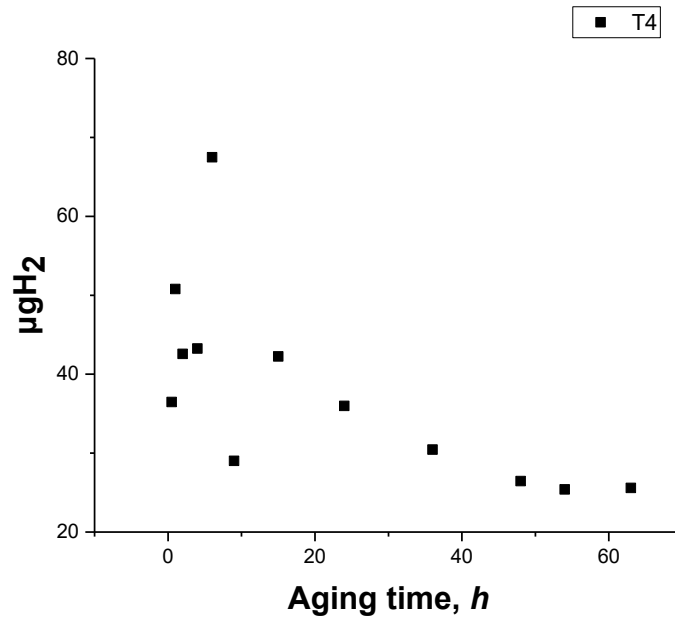
Fig.4 39: Total hydrogen content of corroded specimens in the T4 trapping state as a function of aging time (4 hours in the exfoliation solution, aging temperature 210°C).

# Chapter 5 - Conclusions

Several conclusions were reached after the analysis of results and the discussion in the previous chapter regarding corrosion-induced hydrogen embrittlement in Al-alloy 2024-T351:

1. Precipitate free zones were observed along the grain boundaries of specimens of alloy 2024 when aged at 210°C for varying times with respect to the as received material. These areas affect corrosion behavior of the material studied as well as hydrogen uptake.

2. Exposure to the corrosive solution results in more severe attack with the increase of aging time at a stable time of exposure (4 hours). As the aging time increases the effect on the mechanism of corrosion changes and from pitting to exfoliation.

3. The depth of attack increases with aging time.

4. Experiments concerning hydrogen desorption from alloy 2024-T351 after exposure to the EXCO corrosive solution were in accordance with previous work and the results are reproducible. Hydrogen is produced during the corrosion process and is being trapped in distinct energy states, which correspond to different microstructural traps. These traps are activated and liberate hydrogen at different temperatures. In alloy 2024, four traps T1 to T4 were identified. Trap T1 is considered to be a reversible trap, which liberates hydrogen continuously at low temperatures. Traps T2, T3 and T4 saturate with exposure time and are considered to be irreversible.

5. Trapping state T1 corresponds to hydrogen at interstitial sites. Trapping state T4 is the strongest trap and its temperature range corresponds to the dissolution of the strengthening precipitate in alloy 2024.

6. The study of artificial aging for alloy 2024 revealed that after solid solution and aging at 170°C the maximum peak for the mechanical properties (microhardness) of the alloy is reached after aging between 9 and 15 hours. A less prominent peak is also apparent after 54h of aging.

7. After aging at 210°C the maximum peak for the mechanical properties (microhardness) of the alloy is reached after aging between 4 and 9 hours.

8. The behavior of the T2 trapping state is connected to the peak hardness of the materials. Hydrogen is attracted to the strain fields associated with coherent and semi-coherent interfaces. As the particle size increases with aging time, the hardness increases due to coherency hardening, at the same time $H_2$ increases. After the peak, the interfaces loose coherency and the strain fields diminish. The hardness drops and follows Orowan-mechanism. Hydrogen absorbed for aging at 210°C is less than in the case of 170°C

9.  It has been discussed in previous work that, T3 is associated with dislocation. Coherent / semicoherent interfaces are made up of dislocation arrays. As the particle size increases with aging time, the density of interfacial dislocation increases leading to increase in $H_2$ with aging time. After the peak, the coherency is lost and the density of interfacial dislocation is reduced leading to a reduction of trapping hydrogen.
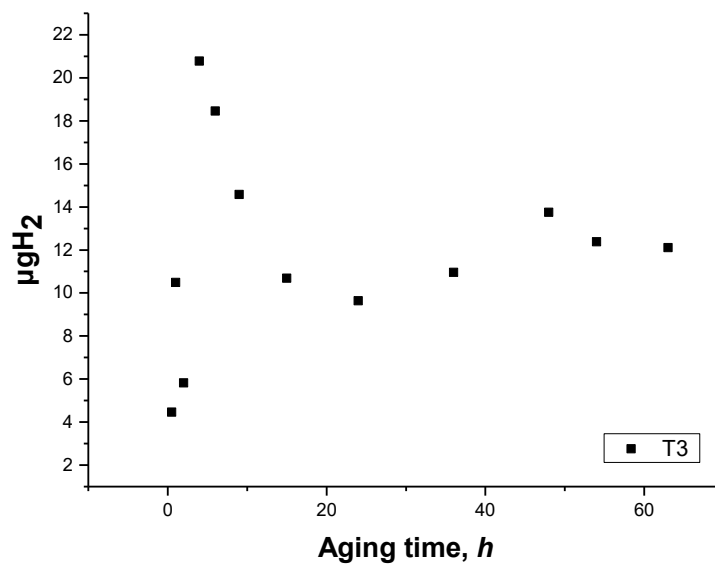
10. Trapping state T4 which is the strongest trap and its temperature range corresponds to the dissolution of the strengthening precipitate in alloy 2024, is associated with S particles. During aging at $210^oC$ the super saturation of solid solution is smaller than when aging at $170^oC$, thus the anticipated volume fraction of the S phase is also smaller.

# Chapter 6 – Proposed Future Work

Taking into consideration the conclusions reached with this thesis the following items are proposed for further investigation:

1. Extensive microstructural study of aluminum alloy 2024-T351 after aging at 170°C.

2. Corrosion induced hydrogen embrittlement study of artificial aging heat treatments at different temperatures, such as 80°C, 120°C, 150°C and 190°C, which would result to different precipitate combinations.

3. Microstructural analysis of the current and future heat treatments by means of Transmission Electron Microscopy and dilatometric measurements.

# References

1. *AGARD Workshop.* 1998, 5-9 October. Corfu, Greece.
2. *BRITE / EURAM No. 1053.* in *ICAF '99 Conference.* 1999. Bellevue, WA.
3. FAA-NASA. 1996. Atlanta, Georgia: National Technical Information Service, Springfield.
4. Speidel, M.O., *Hydrogen embrittlement and stress corrosion cracking of aluminum alloys*, in *Hydrogen Embrittlement and Stress Corrosion Cracking*, R. Gibala and R.F. Heheman, Editors. 1992, ASM: Materials Park, OH,. p. 271-296.
5. De Jong, H.F., *Influence of environmental and temperature on the stress corrosion crack growth rate of aluminum 7075.* Aluminum, 1982. **58**: p. 526-531.
6. Inman, M.E., et al. in *FAA-NASA Symposium on the Continued Airworthiness of Aircraft Structures.* 1996. Atlanta, Georgia: National Technical Information Service, Springfield, Virginia.
7. Pantelakis, S.G., N.I. Vassilas, and P.G. Daglaras, *Effect of corrosive environment on the mechanical behavior of the advanced Al-Li alloys 2091 and 8090 and the conventional aerospace alloy 2024.* METAL, 1993. **47**: p. 135-141.
8. Pantelakis, S.G., P.G. Daglaras, and C.A. Apostolopoulos, *Tensile and energy density properties of 2024, 6013, 8090 and 2091 aircraft aluminum alloy after corrosion exposure.* J. Theor. Appl. Mech., 2000. **33**: p. 117-134.
9. Kamoutsi, H., et al., *Corrosion-induced hydrogen embrittlement in aluminum alloy 2024.* Corrosion Science, 2006. **48**(5): p. 1209-1224.
10. Kamoutsi, H., et al., *Hydrogen Trapping: Deformation and Heat Treatment Effects in 2024 Alloy.* 2006: p. 1293-1294.
11. Kamoutsi, H., et al., *Effect of prior deformation and heat treatment on the corrosion-induced hydrogen trapping in aluminium alloy 2024.* Corrosion Science, 2014. **80**: p. 139-142.
12. Shih, H.-C., N.-J. Ho, and J.C. Huang, *Precipitaion behaviors in Al-Cu-Mg and 2024 aluminum alloys.* Metallurgical and Materials Transactions A, 1996. **27A**: p. 2479-2494.
13. Bigot, A., et al., *3D reconstruction and analysis of GP zones in Al-1.7Cu (at%): A tomographic atom probe investigation.* Applied Surface Science, 1996. **94/95**: p. 261-266.
14. Karlik, M. and B. Jouffrey, *High resolution electron microscopy study of Guinier-Preston (GP1) zones in Al-Cu based alloys.* Acta Materialia, 1997. **45**(8): p. 3251-3263.
15. Karlik, M., B. Jouffrey, and S. Belliot, *The copper content of Guinier-Preston (GP1) zones in Al-1.84 at.% Cu alloy.* Acta Materialia, 1998. **46**(5): p. 1817-1825.
16. Charai, A., et al., *Coexistence of clusters, GPB zones, S''-, S'- and S-phases in an Al-0.9% Cu-1.4% Mg alloy.* Acta Materialia, 2000. **48**(10): p. 2751-2764.
17. Radmilovic, V., et al., *Structure and morphology of S-phase precipitates in aluminum.* Acta Materialia, 1999. **47**(15-16): p. 3987-3997.
18. Ringer, S.P. and K. Hono, *Microstructural evolution and age hardening in Aluminium Alloys; Atom Probe Field-Ion Microscopy and Transmission Electron Microscopy Studies.* Materials Characterization, 2000. **44**(1-2): p. 101-131.
19. Ringer, S.P., B.C. Muddle, and I.J. Polmear, *Effects of cold work on precipitation in Al-Cu-Mg-(Ag) and Al-Cu-Li-(Mg-Ag) alloys.* Metallurgical and Materials Transactions A, 1995. **26A**: p. 1659-1671.
20. Skrotzki, B., G.J. Shiflet, and E.A. Starke, JR., *On the effect of stress on nucleation and growth of precipitates in an Al-Cu-Mg-Ag alloy.* Metallurgical and Materials Transactions A, 1996. **27A**: p. 3431-3444.
21. Ringer, S.P., et al., *Precipitation processes during the early stages of ageing in Al-Cu-Mg alloys.* Applied Surface Science, 1996. **94**(95): p. 253-260.
22. Ringer, S.P., T. Sakurai, and I.J. Polmear, *Origins of Hardening in Aged Al-Cu-Mg-(Ag) Alloys.* Acta Materialia, 1997. **45**(9): p. 3731-3744.
23. Ringer, S.P., G.C. Quan, and T. Sakurai, *Solute clustering, segregation and microstructure in high strength low alloy Al-Cu-Mg alloys.* Materials Science & Engineering A, 1998. **A250**: p. 120-126.

24. Polmear, I.J., *Light Alloys*. Third ed. Metallurgy and Materials Science Series, ed. R. Honeycombe and P. Hancock. 1995, London: Arnold. 362.

25. Davis, J.R., *ASM specialty handbook: Aluminum and Aluminum Alloys*, ed. J.R. Davis. 1993: ASM International.

26. Obispo, H.M., et al., *Copper deposition during the corrosion of aluminum alloy 2024 in sodium chloride solutions.* Journal of Materials Science, 2000. **35**(14): p. 3479-3495.

27. Liao, C.-M. and R.P. Wei, *Galvanic coupling of model alloys to aluminum — a foundation for understanding particle-induced pitting in aluminum alloys.* Electrochimica Acta, 1999. **45**(6): p. 881-888.

28. Buchheit, R.G., *Local Dissolution Phenomena Associated with S Phase (Al$_2$CuMg) Particles in Aluminum Alloy 2024-T3.* Journal of The Electrochemical Society, 1997. **144**(8): p. 2621.

29. Liao, C.-M., et al., *In-situ monitoring of pitting corrosion in aluminum alloy 2024.* Corrosion, 1998. **54**(6): p. 451-458.

30. ASM, *Corrosion of Aluminum and Aluminum Alloys*, ed. J.R. Davis. 1999: ASM International.

31. Foley, R.T., *Localized Corrosion of Aluminum-Alloys - a Review.* Corrosion, 1986. **42**(5): p. 277-288.

32. Gao, M., C.R. Feng, and R.P. Wei, *An analytical electron microscopy study of constituent particles in commercial 7075-T6 and 2024-T3 alloys.* Metallurgical and Materials Transactions A, 1998. **29A**: p. 1145-1151.

33. Shao, M., et al., *A study on pitting corrosion of aluminum alloy 2024-T3 by scanning microreference electrode technique.* Materials Science and Engineering: A, 2003. **344**(1-2): p. 323-327.

34. Blanc, C., B. Lavelle, and G. Mankowski, *The role of precipitates enriched with copper on the susceptibility to pitting corrosion of the 2024 aluminium alloy.* Corrosion Science, 1997. **39**(3): p. 495-510.

35. Sugimoto, K., et al., *Stress corrosion cracking of aged Al-4%Cu alloy in NaCl solution.* Corrosion Science, 1975. **15**(6-12): p. 709-720.

36. Urushino, K. and K. Sugimoto, *Stress-corrosion cracking of aged Al-Cu-Mg alloys in NaCl solution.* Corrosion Science, 1979. **19**(4): p. 225-236.

37. Garner, A. and D. Tromans, *Direct Observation of Intergranular Corrosion in AI-4 Wt% Cu Alloy.* Corrosion, 1979. **35**(2): p. 55-60.

38. Guillaumin, V. and G. Mankowski, *Localized corrosion of 2024 T351 aluminium alloy in chloride media.* Corrosion Science, 1999. **41**: p. 421-438.

39. Burleigh, T.D., *The Postulated Mechanisms for Stress Corrosion Cracking of Aluminum Alloys: A Review of the Literature 1980-1989.* Corrosion, 1991. **47**(2): p. 89-98.

40. Galvele, J.R. and S.M. de De Micheli, *Mechanism of intergranular corrosion of Al-Cu alloys.* Corrosion Science, 1970. **10**(11): p. 795-807.

41. Guillaumin, V. and G. Mankowski, *Localized corrosion of 2024 T351 aluminium alloy in chloride media.* Corrosion Science, 1998. **41**(3): p. 421-438.

42. *Corosion of Aluminum and aluminum alloys*, ed. J.R. Davis.

43. Braun, R., *Exfoliation corrosion testing of aluminium alloys.* British Corrosion Journal, 1995. **30**(3): p. 203-208.

44. Braun, R. in *Aluminium Alloys- Their physical and mechanical properties (ICAA4)*. 1994. Atlanta.

45. Charitidou, E., et al., *Characterization of trapped hydrogen in exfoliation corroded aluminium alloy 2024.* Scripta Materialia, 1999. **41**(12): p. 1327-1332.

46. Haidemenopoulos, G.N., et al., *Hydrogen absorption into aluminum alloy 2024-T3 during exfoliation and alternate immersion testing.* Corrosion, 1998. **54**(1): p. 73-78.

47. Cui, Z.Y., et al., *Exfoliation Corrosion Behavior of 2B06 Aluminum Alloy in a Tropical Marine Atmosphere.* Journal of Materials Engineering and Performance, 2014. **24**(1): p. 296-306.

48. Speidel, M.O., *Hydrogen embrittlement and stress corrosion cracking of aluminum alloys.* Acta Metallurgica, 1974. **22**(9): p. 1057-1183.

49. Tanguy, D., et al., *Hydrogen effects during IGSCC of pure Al-5Mg alloy in NaCl media.* Corrosion Science, 2002. **44**(6): p. 1163-1175.

50. Delafosse, D. and T. Magnin, *Hydrogen induced plasticity in stress corrosion cracking of engineering systems.* Eng. Fract. Mech, 2001. **68**: p. 693-729.

51. Bobby-Kannan, M., et al., *Influence of Multistep Aging on the Stress Corrosion Cracking Behavior of Aluminum Alloy 7010.* Corrosion, 2003. **59**(10): p. 881-889.

52. Lynch, S.P., *Mechanisms of environmentally assisted cracking in AlZnMg single crystals.* Corrosion Science, 1982. **22**(10): p. 925-937.

53. Christodoulou, L. and H.M. Flower, *Hydrogen embrittlement and trapping in Al-6%-Zn-3%-Mg.* Acta Metallurgica, 1980. **28**: p. 481-487.

54. Scamans, G.M., R. Alani, and P.R. Swann, *Pre-Exposure Embrittlement and Stress-Corrosion Failure in Al-Zn-Mg Alloys.* Corrosion Science, 1976. **16**(7): p. 443-459.

55. Kannan, M.B., V.S. Raja, and A.K. Mukhopadhyay, *Determination of true stress corrosion cracking susceptibility index of a high strength Al alloy using glycerin as the non-corrosive atmosphere.* Scripta Materialia, 2004. **51**(11): p. 1075-1079.

56. Scamans, G.M. and C.D.S. Tuck. *Embrittlement of Aluminium Alloys Exposed to Water Vapour*. in *Environment- sensitive fracture of engineering materials*. 1979. New York, NY: Metallurgical Sociaty AIME.

57. Young, G.A. and J.R. Scully, *The Effects of Test Temperature, Temper, and Alloyed Copper on the Hydrogen-Controlled Crack Growth Rate of an Al-Zn-Mg-(Cu) Alloy.* Metallurgical and Materials Transactions A, 2002. **33A**(1): p. 101-115.

58. Jones, R.H., *The influence of hydrogen on the stress-corrosion cracking of low-strength Al-Mg alloys.* Jom, 2003. **55**(2): p. 42-46.

59. *ASTM G34-90*, in *Annual Book of ASTM Standards*, ASTM, Editor. 1994. p. 129.

60. Revie, R.W., et al., *Hydrogen-induced cracking of linepipe steels Part 1-threshold hydrogen concentration and pH.* Corrosion, 1993. **49**(1): p. 17-23.

61. Cantwell, J.E., *High-Temperature hydrogen attack.* Materials Performance, 1994: p. 58-61.

62. Symons, D.M., *The effect of hydrogen on the fracture toughness of alloy X-750 at elevated temperatures.* Journal of Nuclear Materials, 1999. **265**: p. 225-231.

63. Nakamura, M. and K.W. Gao, *Hydrogen embrittlement of Ti-49Al at various strain rates.* Intermetallics, 2002. **10**: p. 233-238.

64. Beachem, C.D., *A new model for hydrogen-assisted cracking (hydrogen "embrittlement").* Metallurgical Transactions, 1972. **3**(2): p. 441-455.

65. Birnbaum, H.K. and P. Sofronis, *Hydrogen-enhanced localized plasticity—a mechanism for hydrogen-related fracture.* Materials Science and Engineering: A, 1994. **176**(1-2): p. 191-202.

66. Robertson, I.M. and H.K. Birnbaum, *An Hvem Study of Hydrogen Effects on the Deformation and Fracture of Nickel.* Acta Metallurgica, 1986. **34**(3): p. 353-366.

67. Tabata, T. and H.K. Birnbaum, *Direct observations of hydrogen enhanced crack propagation in iron.* Scripta Metallurgica, 1984. **18**(3): p. 231-236.

68. Ferreira, P.J., I.M. Robertson, and H.K. Birnbaum, *Hydrogen effects on the interaction between dislocations.* Acta Materialia, 1998. **46**(5): p. 1749-1757.

69. Lu, G., et al., *Hydrogen-enhanced local plasticity in aluminum: an ab initio study.* Phys Rev Lett, 2001. **87**(9): p. 095501.

70. Lynch, S., *Hydrogen embrittlement phenomena and mechanisms.* Corrosion Reviews, 2012. **30**(3-4).

71. Hara, M., et al., *Formation and desorption of aluminum hydride from hydrogen adsorbed aluminum surfaces.* Surface Science, 1991. **242**(1-3): p. 459-463.

72. Ciaraldi, S.W., et al., *Studies of Hydrogen Embrittlement and Stress Corrosion Cracking in an Al–Mg Alloy*, in *H in Metals*. 1980, TMS: Warrenton, PA,. p. 437–447.

73. Buckley, C.E., et al., *Characterization of H defects in the aluminium–hydrogen system using small-angle scattering techniques.* Journal of Applied Crystallography, 2001. **34**(2): p. 119-129.

74. Azofeifa, D.E., et al., *Determination of hydrogen absorption in Pd coated Al thin films.* Thin Solid Films, 1997. **300**(1-2): p. 295-298.

75. Saitoh, H., Y. Iijima, and K. Hirano, *Behaviour of hydrogen in pure aluminium Al-4 mass% Cu and Al-1 mass% Mg₂Si alloys studied by tritium electron microautoradiography.* Journal of Materials Science, 1994. **29**: p. 5739-5744.

76. Itoh, G., K. Koyama, and M. Kanno, *Evidence for the transport of impurity hydrogen with gliding dislocation in aluminum.* Scripta Materialia, 1996. **35**(6): p. 695-698.

77. Pressouyre, G.M., *A classification of hydrogen traps in steel.* Materials Transactions A, 1979. **10A**: p. 1571-1573.

78. Young Jr, G.A. and J.R. Scully. *Hydrogen production, absorption and transport during environment assisted cracking of an Al–Zn–Mg-(Cu) alloy in humid air,.* in *Hydrogen Effects on Materials Behavior and Corrosion Deformation Interactions*. 2003. Jackson Hole, WY.

79. Birnbaum, H.K., et al., *Hydrogen in aluminum.* Journal of Alloys and Compounds, 1997. **253-254**: p. 260-264.

80. Oudriss, A., et al., *Grain size and grain-boundary effects on diffusion and trapping of hydrogen in pure nickel.* Acta Materialia, 2012. **60**(19): p. 6814-6828.

81. Turnbull, A., R.B. Hutchings, and D.H. Ferriss, *Modeling of thermal desorption of hydrogen from metals.* Materials Science & Engineering A, 1997. **238**: p. 317-328.

82. Young, G.A. and J.R. Scully, *The diffusion and trapping of hydrogen in high purity aluminum.* Acta Materialia, 1998. **46**(18): p. 6337-6349.

83. Oudriss, A., et al., *The diffusion and trapping of hydrogen along the grain boundaries in polycrystalline nickel.* Scripta Materialia, 2012. **66**(1): p. 37-40.

84. Izumi, T. and G. Itoh, *Thermal Desorption Spectroscopy Study on the Hydrogen Trapping States in a Pure Aluminum.* Materials Transactions, 2011. **52**(2): p. 130-134.

85. Outlaw, R.A., D.T. Peterson, and F.A. Schmidt, *Hydrogen partitioning in pure cast aluminum as determined by dynamic evolution rate measurements.* Metallurgical Transactions A, 1981. **12**(10): p. 1809-1816.

86. Anyalebechi, P.N., *Hydrogen diffusion in Al-Li alloys.* Metallurgical Transactions B, 1990. **21**(4): p. 649-655.

87. Smith, S.W. and J.R. Scully, *The identification of hydrogen trapping states in an Al-Li-Cu-Zr alloy using thermal desorption spectroscopy.* Metallurgical and Materials Transactions A, 2000. **31**(1): p. 179-193.

88. Hadam, U. and T. Zakroczymski, *Absorption of hydrogen in tensile strained iron and high-carbon steel studied by electrochemical permeation and desorption techniques.* International Journal of Hydrogen Energy, 2009. **34**(5): p. 2449-2459.

89. Frappart, S., et al., *Study of the hydrogen diffusion and segregation into Fe–C–Mo martensitic HSLA steel using electrochemical permeation test.* Journal of Physics and Chemistry of Solids, 2010. **71**(10): p. 1467-1479.

90. Pérez Escobar, D., et al., *Thermal desorption spectroscopy study of the interaction between hydrogen and different microstructural constituents in lab cast Fe–C alloys.* Corrosion Science, 2012. **65**: p. 199-208.

91. Foster, L.M., T.H. Jack, and W.W. Hill, *Structures revealed in zone refined aluminum by tritium decoration.* Metallurgical Transactions, 1970. **1**: p. 3117-3124.

92. Lee, S.-M. and J.-Y. Lee, *The trapping and transport phenomena of hydrogen in nickel.* Metallurgical Transactions A, 1986. **17A**: p. 181-187.

93. Diao, Y., M. Cao, and X. Wan, *Hydrogen Trapping by Dislocations and Grain Boundaries in Fe-3%Si Alloy.* J. Mater. Sci. Technol., 1993. **9**(5): p. 385-387.

94. Ai, J.-H., et al., *Hydrogen diffusion and trapping in a precipitation-hardened nickel–copper–aluminum alloy Monel K-500 (UNS N05500).* Acta Materialia, 2013. **61**(9): p. 3186-3199.

95. Iijima, Y., et al., *Hydrogen trapping and repelling in an Al-6 wt % Zn-2 wt % Mg alloy.* Journal of Materials Science, 1992. **27**(21): p. 5735-5738.

96. El-Amoush, A.S., *An investigation of hydrogen-induced hardening in 7075-T6 aluminum alloy.* Journal of Alloys and Compounds, 2008. **465**(1-2): p. 497-501.

97.  Guérin, M., et al., *Effect of varying conditions of exposure to an aggressive medium on the corrosion behavior of the 2050 Al–Cu–Li alloy.* Corrosion Science, 2014. **85**: p. 455-470.

98.  Sofronis, P., Y. Liang, and N. Aravas, *Hydrogen induced shear localization of the plastic flow in metals and alloys.* European Journal of Mechanics a-Solids, 2001. **20**(6): p. 857-872.

99.  Liang, Y., P. Sofronis, and R.H. Dodds, *Interaction of hydrogen with crack-tip plasticity: effects of constraint on void growth.* Materials Science and Engineering: A, 2004. **366**(2): p. 397-411.

100. Parvizi, R., et al., *Atom probe tomography study of the nanoscale heterostructure around an Al20Mn3Cu2 dispersoid in aluminum alloy 2024.* Langmuir, 2014. **30**(49): p. 14817-23.

101. Scherer, J., et al., *Initial stages of the anodic etching of aluminium foils studied by atomic force microscopy.* Corrosion Science, 1999. **41**: p. 35-55.

102. Alexopoulos, N.D., et al., *The effect of artificial ageing heat treatments on the corrosion-induced hydrogen embrittlement of 2024 (Al–Cu) aluminium alloy.* Corrosion Science, 2016. **102**: p. 413-424.

103. Floratos, P., H. Kamoutsi, and G. Haidemenopoulos. *Effect of aging treatment on the corrosion-induced hydrogen trapping in AA2024*. in *5th Panhellenic Conference on Metallic Materials*. 2016. Giannena, Greece.